Thermodynamic signatures of quantum criticality in cuprate superconductors

B. Michon[1,2,3], C. Girod[1,2,3], S. Badoux[2], J. Kačmarčík[4], Q. Ma[5], M. Dragomir[6], H. A. Dabkowska[6], B. D. Gaulin[5,6,7], J.-S. Zhou[8], S. Pyon[9], T. Takayama[9], H. Takagi[9], S. Verret[2], N. Doiron-Leyraud[2], C. Marcenat[10], L. Taillefer[2,7], T. Klein[1,3]

1 Univ. Grenoble Alpes, Institut Néel, F-38042 Grenoble, France

2 Institut quantique, Département de physique & RQMP, Université de Sherbrooke, Sherbrooke, Québec J1K 2R1, Canada

3 CNRS, Institut Néel, 38042 Grenoble, France

4 Institute of Experimental Physics, Slovak Academy of Sciences, SK-04001 Košice, Slovakia

5 Department of Physics and Astronomy, McMaster University, Hamilton, Ontario L8S 4M1, Canada

6 Brockhouse Institute for Materials Research, McMaster University, Hamilton, Ontario L8S 4M1, Canada

7 Canadian Institute for Advanced Research, Toronto, Ontario M5G 1Z8, Canada

8 Materials Science and Engineering Program, Mechanical Engineering, University of Texas at Austin, Austin, Texas 78712, USA

9 Department of Advanced Materials, University of Tokyo, Kashiwa 277-8561, Japan

10 Univ. Grenoble Alpes, CEA, INAC, PHELIQS, LATEQS, F-38000 Grenoble, France

The three central phenomena of cuprate superconductors are linked by a common doping *p – where the enigmatic pseudogap phase ends and the resistivity exhibits an anomalous linear dependence on temperature, and around which the**

superconducting phase forms a dome (ref. 1). However, the fundamental nature of *p remains unclear, in particular whether it marks a true quantum phase transition. We have measured the specific heat *C* of the cuprates Eu-LSCO and Nd-LSCO at low temperature in magnetic fields large enough to suppress superconductivity, over a wide doping range across *p** (ref. 2). As a function of doping, we find that the electronic term C_{el} / *T* is strongly peaked at *p**, where it exhibits a log(1/*T*) dependence as $T \rightarrow 0$. These are the classic signatures of a quantum critical point[3,4,5], as observed in heavy-fermion[6] and iron-based[7] superconductors where their antiferromagnetic phase ends. We conclude that the pseudogap phase of cuprates ends at a quantum critical point, whose associated fluctuations are most likely involved in the *d*-wave pairing and the anomalous scattering.**

In the phase diagram of several organic, heavy-fermion and iron-based superconductors, superconductivity forms a dome around the quantum critical point (QCP) where a phase of antiferromagnetic (AF) order ends. The spin fluctuations associated with that QCP are believed to cause both pairing and scattering[4]. The scattering is anomalous in that it produces a resistivity with a linear temperature dependence as $T \rightarrow 0$, instead of the conventional T^2 dependence of a Fermi liquid[3,5,8]. In hole-doped cuprates, these same features – a T_c dome and a *T*-linear resistivity – are also observed[1], but not at the critical doping where the Néel temperature T_N for the onset of long-range AF order vanishes. Instead, they are observed near the doping *p** where the pseudogap phase ends (Extended Data Fig. 1) and the essential nature of this phase remains unknown – it is the central enigma of cuprates.

The thermodynamic signature of a QCP is a diverging electronic mass. For an AF QCP in two dimensions, for example, the mass is expected to go as $m^* \sim \log(1/|x-x^*|)$ and the specific heat *C* as $C / T \sim \log(1/|x-x^*|)$, as one moves the system towards its QCP at x^* by varying some tuning parameter *x*, such as pressure or concentration[3]. This is what is observed in the iron-based superconductor $BaFe_2(As_{1-x}P_x)_2$ at its AF QCP (tuned by P concentration), both in the carrier mass m^* measured via quantum oscillations and in the electronic specific heat estimated from the jump at T_c (refs. 5,7). At $x = x^*$, one expects that $C / T \sim \log(1/T)$, as observed in the heavy-fermion metal $CeCu_{6-x}Au_x$ at its AF QCP (tuned by Au concentration) (refs. 3,6). This logarithmic divergence of C / T as $T \rightarrow 0$ is the true sign of an energy scale that vanishes at x^*.

In the cuprate $YBa_2Cu_3O_y$ (YBCO), a study of quantum oscillations[9] has revealed an increase in m^* as p approaches the pseudogap critical doping $p^* \sim 0.19$, suggesting that p^* may be a QCP. The low value of m^* at $p = 0.10 – 0.12$ is consistent with specific heat data[10] (*modulo* a residual value attributed to CuO chains) and its increase vs p is consistent with the dramatic increase in the magnitude of the specific heat jump at T_c, $\Delta C / T_c$ (refs. 11,12), which reaches its maximal value at p^* (Fig. 1). However, to conclude that there is quantum criticality, what is missing is a direct measurement of the normal-state specific heat of a cuprate as $T \to 0$, across p^*. This is what we report here.

We have measured $C(T)$ in the closely related cuprate materials $La_{1.8-x}Eu_{0.2}Sr_xCuO_4$ (Eu-LSCO) and $La_{1.6-x}Nd_{0.4}Sr_xCuO_4$ (Nd-LSCO). Because of their low T_c (< 20 K), superconductivity can be fully suppressed with a readily accessible magnetic field (~ 15 T). The two materials have the same crystal structure and phase diagram, with very similar boundaries for the pseudogap phase, $T^*(p)$ (Extended Data Fig. 1), and superconducting phase, $T_c(p)$ (Extended Data Fig. 2). In Nd-LSCO, resistivity and Hall effect measurements yield $p^* = 0.23 \pm 0.01$ (ref. 2). At $p = 0.24$, $\rho(T)$ is linear in T as $T \to 0$, the signature of quantum criticality in electrical transport. A very similar behavior is observed in Eu-LSCO (Extended Data Fig. 2). We deduce that $p^* \sim 0.23$ also in Eu-LSCO.

The specific heat of 5 crystals of Eu-LSCO and 7 crystals of Nd-LSCO was measured below 10 K (Supplementary Fig. S1). The normal-state specific heat is obtained by applying a magnetic field of either $H = 8$ T or 18 T (Extended Data Figs. 3, 4). In Figs. 2a and 2c, we show normal-state data at $H = 18$ T in Eu-LSCO and Nd-LSCO, respectively, plotted as C / T vs T^2. Note that the magnetic moment on the Nd produces a Schottky anomaly in the specific heat of Nd-LSCO (C_{mag}), not present in Eu-LSCO (since Eu has no moment). At $H = 0$, this anomaly leads to a large increase of C / T at low T. However, a magnetic field moves this Schottky contribution to higher temperature, so that it becomes negligible below ~ 5 K at 18 T (Extended Data Fig. 5c).

In Fig. 3a, we plot the raw data at $T = 2$ K (and $H = 18$ T), C / T vs p, for all 12 crystals. The 12 data points fall on the same smooth curve, demonstrating a high level of quantitative fidelity and reproducibility. Because the magnetic and nuclear Schottky contributions (C_{mag} and $C_{nuclear}$; see Methods) are both negligible at 2 K, we have

$C = C_{el} + C_{ph}$, the sum of electronic and phononic contributions. In Eu-LSCO at $p = 0.11$ and $p = 0.16$, the data obey $C / T = \gamma + \beta T^2$ below $T \sim 5$ K (Fig. 2a). The residual linear term γ is electronic and the second term is due to phonons, with $\beta \sim 0.22$ mJ / K^4 mol for both dopings. The same is true in Nd-LSCO at $p = 0.12$ (Fig. 2c) and $p = 0.15$ (Supplementary Fig. S1c), again with $\beta \sim 0.22$ mJ / K^4 mol for both dopings. In Extended Data Fig. 6d, we plot β vs p for all our samples. We see that beta is constant between $p = 0.1$and $p = 0.4$, within error bars, as that C_{ph} / T is a small constant background in that range (dashed lines in Fig. 3a).

To investigate what happens above p^*, we measured the specific heat of three Nd-LSCO samples with $p = 0.27$, 0.36 and 0.40 – dopings at which the material is no longer superconducting. Because it is difficult to grow single crystals at such high doping, the samples are polycrystalline powder. As a result, a field cannot be used to shift the magnetic Schottky anomaly (C_{mag}) up in temperature (because the effect of a field is highly anisotropic). Nevertheless, we can reliably subtract C_{mag} from C and obtain $C_{el} + C_{ph}$, as demonstrated in Extended Data Figs. 7 and 8 for our five polycrystalline samples. In all cases, the zero-field data obey $(C - C_{mag})/T = \gamma + \beta T^2$, with values of γ and β that are consistent with those obtained in single crystals. In Extended Data Fig. 7a, we show that polycrystalline and single-crystal samples yield the exact same data, at the same doping (here $p = 0.12$). Plotting the values of $(C - C_{mag})/T$ at $T = 2$ K in Fig. 3a, we see that C / T drops by a factor 3 in going from p^* up to $p = 0.4$. Our values in Nd-LSCO are consistent with published data on $La_{2-x}Sr_xCuO_4$ (LSCO) at $p = 0.33$ (ref. 13) (Fig. 3a).

The thermodynamic signature of the pseudogap critical point in Eu-LSCO and Nd-LSCO is therefore seen to be a huge peak in C_{el} / T at p^*, at low temperature, not just a drop below p^* (Fig. 3a). There are two standard explanations for such a peak: a van Hove singularity (vHs) in the band structure and a quantum critical point. Because there is indeed a vHs in Nd-LSCO at $p = p_{vHs} \sim p^*$ (ref. 14), we have considered the first scenario carefully. Fortunately, the band structure of Nd-LSCO is well known and simple[14], so reliable calculations can be performed. In a perfectly clean two-dimensional metal, C_{el} / T vs p does show a sharp cusp at $p = p_{vHs}$ in the $T = 0$ limit (Extended Data Fig. 9). However, when the actual 3D dispersion of the real Fermi surface and the actual level of disorder scattering of the real samples are included, the peak due to the vHs is dramatically reduced and broadened (Extended Data Fig. 9). The large and sharp peak we observe is therefore clearly due to electronic effects beyond the band structure.

We now turn to the temperature dependence of C_{el}. In Fig. 2a, we see that C / T at $p = 0.24$ deviates strongly from the $\gamma + \beta T^2$ behavior as $T \rightarrow 0$. To investigate this deviation in detail, measurements were carried out in a ^{3}He refrigerator with a field of 8 T, just enough to reach the normal state at $p = 0.16$ and 0.24 (Extended Data Fig. 4). The data are plotted as C / T vs T in Extended Data Fig. 5a. Below 1 K, we observe a nuclear Schottky anomaly ($C_{nuclear}$), which rises as $C / T \sim T^{-3}$. Because $C_{nuclear}$ and C_{ph} are both almost independent of doping, we can readily subtract them from the measured C and obtain the purely electronic contribution C_{el} (see Methods). The result is plotted as C_{el} / T vs $\log T$ in Fig. 2b. At $p = 0.11$, we see that C_{el} / T is constant, with $C_{el} / T = \gamma =$ 2.8 mJ /K^2 mol. By contrast, at $p = 0.24$, we see that C_{el} / T grows linearly from ~ 10 K all the way down to 0.5 K, our lowest temperature. We arrive at the key finding that $C_{el} / T \sim \log(1/T)$ at $p \sim p^*$.

The fact that C_{el} / T keeps increasing as $T \rightarrow 0$ at $p = 0.24$ is confirmed directly by looking at $\Delta C / T_c$, the jump in C / T at T_c, the two being linked by entropy balance. In Extended Data Fig. 3, we see that $\Delta C / T_c$ increases by a factor 10 in going from $p = 0.11$ to $p = 0.24$, in tandem with the increase in C_{el} / T at $T = 0.5$ K (Fig. 3b).

In Extended Data Fig. 5d (and Supplementary Fig. S1c), we show Nd-LSCO data obtained in the ^{3}He refrigerator at $H = 8$ T, a field sufficient to suppress superconductivity at $p = 0.12$, 0.22, 0.23, 0.24 and 0.25. As described in the Methods, we obtain $C_{el}(T)$ as we did for Eu-LSCO. The result is displayed in Fig. 2d (and Supplementary Fig. S1d), plotted as C_{el} / T vs $\log T$. The Nd-LSCO data for $C_{el}(T)$ are seen to be in excellent quantitative agreement with the Eu-LSCO data (Fig. 2b). In particular, they confirm our key finding that $C_{el} / T \sim \log(1/T)$ at $p \sim p^*$. We therefore find that the cuprates Eu-LSCO and Nd-LSCO exhibit the classic thermodynamic signature of a QCP, as observed in the AF heavy-fermion metals $CeCu_{6-x}Au_x$ (ref. 6), $YbRh_2Si_2$ (ref. 15), and $CeCoIn_5$ (ref. 16).

In Fig. 3b, we plot the value of C_{el} / T for our 12 crystals as a function of doping, estimated at $T = 0.5$ K. We also plot the extrapolated γ values for our five polycrystalline samples of Nd-LSCO ($p = 0.07$, 0.12, 0.27, 0.36 and 0.40; Extended Data Figs. 7b and 8b) and the LSCO crystal at $p = 0.33$ (ref. 13). The huge cusp-like peak in C_{el} / T vs p is very similar to that seen in the iron-based superconductor $BaFe_2(As_{1-x}P_x)_2$ at its AF QCP, with $C / T \sim \log(1/|x-x^*|)$ (ref. 7). Taken together, the p and T dependences of C_{el} provide compelling evidence for a QCP in Eu-LSCO and Nd-LSCO.

The strong similarity of our data on Nd-LSCO and Eu-LSCO with data on other cuprates indicates that the signatures of a QCP reported here are likely to be a generic feature of hole-doped cuprates. In Extended Data Fig. 10b, we compare our values of C_{el} / T in Eu-LSCO and Nd-LSCO at 10 K (Extended Data Fig. 10a) with γ values in LSCO obtained from fits to $C / T = \gamma + \beta T^2$ between ~ 4 K and ~ 8 K, where C was measured on LSCO powders made non-superconducting by adding high levels of Zn impurities[17]. (Note that in this early work the temperature dependence of C_{el} / T was not investigated at very low temperature.) A clear peak in γ vs p is observed also in LSCO, similar to that found here in Nd-LSCO, although centered at a slightly lower doping – consistent with the lower p^* in that material (Extended Data Fig. 1).

In no other cuprate has a direct measurement of the normal-state specific heat at low temperature been performed across p^*. To continue our survey of cuprates, we must therefore piece together different data from different materials. This is what we do in Fig. 1. Starting on the overdoped side, we have $\gamma = 6.6 \pm 1$ mJ / K^2 mol in $Tl_2Ba_2CuO_{6+\delta}$ (Tl-2201) at $p \sim 0.33$ (ref. 18), not far from $\gamma = 7.6 \pm 0.6$ mJ / K^2 mol obtained from the effective mass measured by quantum oscillations, $m^* = 5.2 \pm 0.4\ m_e$, in Tl-2201 at $p = 0.29 \pm 0.02$ (ref. 19). Since those are similar to the values found in Nd-LSCO and in LSCO at $p \sim 0.3$ (Fig. 3b), it is reasonable to suppose that other cuprates, such as YBCO, $Bi_2Sr_2CaCu_2O_8$ (Bi2212) and $HgBa_2CuO_{4+\delta}$ (Hg-1201), would also have $\gamma \sim 7$ mJ / K^2 mol at $p \sim 0.3$. (In none of these three materials has m^*, γ or $\Delta C / T_c$ been measured beyond $p \sim 0.23$ (refs. 12, 20). Note that $p^* = 0.22$ in Bi2212 (ref. 21).) On the underdoped side, $\gamma \sim 3$ mJ / K^2 mol in YBCO at $p \sim 0.1$ (ref. 10) and quantum oscillations in YBCO (ref. 9) and Hg-1201 (ref. 22) at $p \sim 0.1$ yield $\gamma = 2.5$ and 4.0 mJ / K^2 mol, respectively (per mole of planar Cu), compared to $\gamma = 2.8$ and 3.6 mJ / K^2 mol in Eu-LSCO at $p = 0.11$ and Nd-LSCO at $p = 0.12$, respectively (Fig. 3b) – all in good agreement (Fig. 1).

We emphasize that γ in Tl-2201 at $p \sim 0.33$ is only a factor 1.7 larger than γ in Hg-1201 at $p \sim 0.1$. In other words, the opening of the pseudogap between the two has only reduced the density of states by a factor ~ 1.7. This is a much smaller reduction than that observed in going from p* to p = 0.1 in any hole-doped cuprate[11,12,17,20,23]. If we assume that the reduction below p* in Tl-2201 is comparable to that in other cuprates, then γ in Tl-2201 must first rise from $p \sim 0.33$ to p* before it falls below p*. This would imply that a peak in C_{el}/T at p* is a generic property of cuprates. (Note, however, that the only attempt to extract the doping dependence of γ in Tl-2201, based on zero field data, found a constant γ (ref. 18). A direct measurement of the normal-state C_{el} is needed to resolve this apparent contradiction.)

In Fig. 1, we also plot the specific heat jump at T_c, $\Delta C / T_c$, as a function of p, previously measured in Ca-doped YBCO (ref. 12). We see that $\Delta C / T_c$ drops by a factor ~ 10 in going from p* to $p \sim 0.1$, consistent with the drop in condensation energy[23]. Since $\Delta C / T_c \sim \gamma$, this implies that $\gamma \sim 25$ mJ / K^2 mol at p* in YBCO (Fig. 1), comparable to our value of $C_{el}/T = 22$ mJ / K^2 mol at $T = 0.5$ K in Nd-LSCO at p* (Fig. 3b). This high value of γ in YBCO must then drop by a factor ~ 3-4 above p*, if it is to reach the common value $\gamma \sim 7$ mJ / K^2 mol at $p \sim 0.3$ (Fig. 1). In summary, while further work is needed to establish that there is indeed a peak in C_{el}/T vs p for cuprates other than Nd-LSCO, Eu-LSCO and LSCO, most existing data are not incompatible with a universal peak in hole-doped cuprates.

Our finding that C_{el}/T peaks at p* is a change of paradigm in our understanding of cuprates – it reveals a mechanism of strong mass enhancement above p*, associated with a QCP at p*. Our observation of a continuous logarithmic increase of the electronic specific heat down to temperatures as low as 0.5 K raises the fundamental question of what energy scale, associated with most of the low-temperature entropy, vanishes at p* ? And what corresponding length scale diverges at p* ?

Given the remarkable similarity with the signatures of an AF QCP, as observed in heavy-fermion metals[6] and iron-based superconductors[7], it is tempting to attribute the quantum criticality of cuprates to AF spin correlations. However, unlike in electron-doped cuprates where the AF correlation length diverges as $T \rightarrow 0$ (ref. 24) close to the critical doping x* where the Fermi surface is reconstructed and $\rho(T)$ is T-linear (ref. 25), there is no evidence of a diverging AF correlation length in hole-doped cuprates near p* (ref. 26).

In Nd-LSCO, incommensurate spin-density-wave (SDW) order is observed by neutron diffraction[27] to vanish with increasing p at $p \sim p^*$, but there is no divergent SDW correlation length or vanishing energy scale. Indeed, muon spin relaxation finds that the magnetic order in Nd-LSCO vanishes before p^*, at $p \sim 0.20$, which indicates that the order is not static at $p = 0.20$ (ref. 28), or above.

It may therefore be that the quantum criticality of hole-doped cuprates is of an entirely new kind, possibly involving topological order[29]. Alternatively, we may be dealing with two closely intertwined mechanisms: one mechanism for the pseudogap, possibly short-range AF correlations, and a second – separate but coupled – mechanism for the quantum criticality, possibly nematic order[30] or current-loop order[31].

Acknowledgements. The authors would like to thank J. Chang, M. Horio, M.-H. Julien, S. Kivelson, R. Markiewicz, C. Proust, B. Ramshaw, S. Sachdev, A. Sacuto, J. Tallon, A.-M. Tremblay, and C. Varma for fruitful discussions. C.M. and T.K. acknowledge support from the Laboratoire d'excellence LANEF (ANR-10-LABX-51-01) and the Laboratoire National des Champs Magnétiques Intenses (LNCMI) in Grenoble. L.T. acknowledges support from the Canadian Institute for Advanced Research (CIFAR) and funding from the Natural Sciences and Engineering Research Council of Canada (NSERC; PIN:123817), the Fonds de recherche du Québec - Nature et Technologies (FRQNT), the Canada Foundation for Innovation (CFI), and a Canada Research Chair. This research was undertaken thanks in part to funding from the Canada First Research Excellence Fund. Part of this work was funded by the Gordon and Betty Moore Foundation's EPiQS Initiative (Grant GBMF5306 to L.T.). J.-S.Z was supported by NSF MRSEC under Cooperative Agreement No. DMR-1720595 in the US. H.T. acknowledges MEXT Japan for a Grant-in-Aid for Scientific Research.

Author contributions. B.M., C.G., C.M. and T.K. performed the specific heat measurements. J.K. assisted in the development of the measurement technique. B.M., S.B. and N.D.-L. characterized the samples via resistivity and magnetization measurements. J.-S.Z. prepared the Nd-LSCO crystals. S.P., T.T. and H.T. prepared the Eu-LSCO crystals. Q.M., M.D., H.A.D. and B.D.G. prepared the Nd-LSCO polycrystalline samples and measured the phonon energies of Nd-LSCO with neutron scattering. S.V. calculated the specific heat of Nd-LSCO from its 3D band structure. B.M., C.M., L.T. and T.K. wrote the manuscript, in consultation with all authors. L.T. and T.K. designed the study and supervised the project.

Author information. The authors declare no competing financial interest. Correspondence and requests for materials should be addressed to L.T. (louis.taillefer@usherbrooke.ca) or T.K. (thierry.klein@neel.cnrs.fr).

MAIN FIGURE CAPTIONS

Fig. 1 | Specific heat data in various cuprates.

Electronic specific heat coefficient γ in non-superconducting Tl-2201 at $p = 0.33 \pm 0.02$ (full orange diamond, left axis; ref. 18) and in the field-induced normal state of YBCO at $p = 0.10$, 0.11 and 0.12 (full blue circles, left axis; ref. 10; a background zero-field component attributed to CuO chains is removed from these γ values). Also shown are the values of γ obtained from the effective mass m^* measured by quantum oscillations (QO) in YBCO at $0.08 < p < 0.16$ (open blue circles, left axis; ref. 9), Tl-2201 at $p = 0.29 \pm 0.02$ (open orange diamond, left axis; ref. 19) and Hg-1201 at $p \sim 0.1$ (open green square, left axis; ref. 22). The error bars are from the original papers. The jump in specific heat at T_c, $\Delta C / T_c$ (defined in Extended Data Fig. 3), measured in Ca-doped YBCO (open blue triangles; ref. 12) is plotted for comparison (right axis). (Note that $\Delta C / T_c$ is not a direct measurement of γ, and it is affected by pair breaking due to disorder, more so as T_c decreases.) The doping p is taken from the original papers[9,10,12,19,22], except for Tl-2201 at $p = 0.33$ where it is estimated from the fact that the sample is non-superconducting[18] and the T_c dome ends at $p = 0.31$ (ref. 19). The units are expressed per Cu atom in the CuO_2 planes. The dashed blue line marks the pseudogap critical point p^* in YBCO. The solid line is a guide to the eye.

Fig. 2 | Specific heat of Eu-LSCO and Nd-LSCO.

a) Specific heat of Eu-LSCO measured in a field H = 18 T, plotted as C / T vs T^2, for four different dopings, as indicated. The dashed line is a linear fit to the data at p = 0.11 (blue) for T < 5 K; it yields γ = 2.8 mJ /K^2 mol and β = 0.22 mJ / K^4 mol, where C / T = γ + βT^2. (Data for our 5 crystals of Eu-LSCO are displayed in Supplementary Fig. S1.) **b)** Electronic specific heat of Eu-LSCO, $C_{el}(T)$, obtained as described in the Methods, plotted as C_{el} /T vs log$T$, from data at H = 8 T (p = 0.11 and 0.24) and at H = 18 T (p = 0.21). (The dashed line is a linear extrapolation of the p = 0.21 data.) At p = 0.11, C_{el} / T = γ, a constant, while at p = 0.24 ~ p*, C_{el} / T ~ log(1/T), the thermodynamic signature of a quantum critical point. **c)** Specific heat of Nd-LSCO measured in a field H = 18 T, plotted as C / T vs T^2, for four dopings, as indicated. (Data for our 7 crystals of Nd-LSCO are displayed in Supplementary Fig. S1.) The dashed line is a linear fit to the data at p = 0.12, C / T = γ + βT^2 (below 5 K), giving γ = 3.6 mJ /K^2 mol and β = 0.215 mJ / K^4 mol. **d)** Electronic specific heat of Nd-LSCO, obtained as described in the Methods, plotted as C_{el} /T vs log$T$. This is done separately for the data below (H = 8 T) and above (H = 18 T) the dashed line. At p = 0.24 ~ p*, C_{el}/T ~ log(1/T), just as in Eu-LSCO.

Fig. 3 | Doping dependence of the electronic specific heat.

a) Raw data for C/T in Eu-LSCO (squares) and Nd-LSCO (circles) at T = 2 K and H = 18 T (full red symbols) and at T = 1 K and H = 8 T (full orange squares). We also include data points for non-superconducting LSCO at H = 0 (diamonds), at T = 2 K (red) and T = 1 K (orange), at p = 0.33 (ref. 13). Open circles are (C – C_{mag})/T at T = 2 K obtained on polycrystalline samples of Nd-LSCO (Extended Data Figs. 7, 8). The dashed lines indicate the phonon contribution, C_{ph} /T = βT^2, to the specific heat of Nd-LSCO, at T = 2 K (red) and T = 1 K (orange) (Extended Data Fig. 6d). **b)** Normal-state electronic specific heat C_{el} of Eu-LSCO (squares) and Nd-LSCO (red circles, crystals), at T = 0.5 K, plotted as C_{el} /T vs p (see Extended Data Fig. 10a for details). Error bars are explained in the Methods. We also include γ for Nd-LSCO (purple circles, polycrystals; see Extended Data Figs. 7, 8) and non-superconducting LSCO from published work (diamonds; p < 0.06 (ref. 32), p = 0.33 (ref. 13)), obtained by extrapolating C / T = γ + βT^2 to T = 0 from data below 10 K. The jump in specific heat at T_c , ΔC / T_c , measured in Eu-LSCO (blue triangles; Extended Data Fig. 3) is plotted for comparison (right axis). We see that ΔC / T_c and C_{el} /T scale nicely. The dashed line marks the pseudogap critical point p* in Nd-LSCO (Extended Data Fig. 1). The solid lines are a guide to the eye.

METHODS

SAMPLES

Eu-LSCO. Single crystals of $La_{2-y-x}Eu_ySr_xCuO_4$ (Eu-LSCO) were grown at the University of Tokyo with a Eu content y = 0.2, using a travelling-float-zone technique. Five samples were cut in the shape of small rectangular platelets, of typical dimensions 1 mm × 1 mm × 0.5 mm and mass of ~ 1 mg, from boules with nominal Sr concentrations x = 0.08, 0.11, 0.16, 0.21, and 0.24. The hole concentration p is given by $p = x$, with a maximal error bar of ± 0.005. The critical temperature T_c of our samples, defined as the onset of the drop in the magnetization, is plotted in Extended Data Fig. 2a.

Nd-LSCO. Single crystals of $La_{2-y-x}Nd_ySr_xCuO_4$ (Nd-LSCO) were grown at the University of Texas at Austin with a Nd content y = 0.4, using a travelling-float-zone technique. Seven samples were cut in the shape of small rectangular platelets, of typical dimensions 1 mm × 1 mm × 0.5 mm and mass of ~ 1 mg, from boules with nominal Sr concentrations x = 0.12, 0.15, 0.20, 0.22, 0.23, 0.24 and 0.25. The hole concentration p is given by $p = x$, with an error bar ± 0.003, except for our sample with p = 0.24, for which the error bar is ± 0.005 (ref. 2). The T_c of all samples is plotted in Extended Data Fig. 2b. The rapid decrease in T_c from p = 0.22 to p = 0.25 provides a sensitive measure of the relative doping of samples in that range.

Powder samples of Nd-LSCO were produced at McMaster University with y = 0.4 and x = 0.07, 0.12, 0.27, 0.36 and 0.40, and shaped into sintered pellets. Samples with x = 0.27, 0.36 and 0.40 are not superconducting, and so their normal-state specific heat can be measured in zero field. The uncertainty on p from x is ± 0.01.

SPECIFIC HEAT MEASUREMENTS

To perform the series of specific heat measurements reported in this article, we implemented an original AC modulation method which leads to an absolute accuracy of ΔC / C ~ ± 4 % with a relative sensitivity ΔC / C ~ ± 0.01 % on samples whose masses are on the order of 1.0 mg (down to 0.1 mg). These figures are valid for the temperature range 0.5 K < T < 20 K and for the magnetic field range 0 < H < 18 T.

Calorimetric setup. The calorimetric chips were prepared out of bare Cernox chips (1010 for T < 2 K, 1050 for T > 2 K). First, a shallow groove is made in the central part with a wire saw to obtain two independent films; one used as a heater (of resistance R_h) and the other one as the thermometer (of resistance R_t) (Supplementary Fig. S2). The split chip is thereafter attached to a small copper ring with PtW(7%) wires, 25 or 50 μm in diameter and 1 to 2 mm in length, glued with a minute amount of Ag epoxy. The choice of wires is important since it defines the external thermal conductance and the frequency range where the measurements will have their optimal accuracy (between 0.5 Hz and 20 Hz). We used PtW wires since their thermal conductivity is insensitive to magnetic fields (< 1 % in 18 T).

Modulation technique. In the simplest approximation, when an alternative current I_{ac} is applied at a frequency ω on the heater side, temperature oscillations $T_{ac} = P_{ac} / (K_e + jC2\omega)$ are induced at 2ω, where K_e is the external thermal conductance and C the total heat capacity. Introducing the phase φ of T_{ac} relative to the power P_{ac}, one gets:

$$C = P_{ac} \sin(-\varphi) / [2\omega\, |T_{ac}|]\ ,\ \text{with } P_{ac} = R_h\, |I_{ac}|^2 / 2\ .$$

These oscillations can then be measured by applying a DC current I_{dc} across the thermometer: $V_{ac}^{t}(2\omega) = [(\mathrm{d}R_t / \mathrm{d}T)\ T_{ac}(2\omega)]\ I_{dc}$. The main drawback of this simple approach is that internal time corrections (due to finite thermal conductances between the different parts of the chips: thermometer-heater-substrate-sample) are not taken into account. To overcome this difficulty, especially at the lowest temperature where the thermal conductivity between the sensing layer of the Cernox and the sapphire substrate is the main limiting factor, we have also used the heater side to measure the temperature oscillations: $V_{ac}^{h}(3\omega) = [(\mathrm{d}R_h / \mathrm{d}T)\ T_{ac}(2\omega)]\ I_{ac}(\omega)$.

When all the internal conductances are larger than the external one K_e, the T_{ac} measured on the thermometer side (at 2ω) must be the same as that measured on the heater side (at 3ω). Any difference points to a thermal gradient within the chips, which can then be minimized by adjusting the measurement parameters. This procedure improves the absolute accuracy and enables a much better estimate of the error bars.

Thermometry. The first step is to know precisely the temperature of the main heat sink on which the measuring chip is attached. This is achieved with commercial calibrated Cernox sensors 1010 and 1050, used respectively in the ranges 0.5 – 5 K and 1.5 – 20 K. The calibration has been further improved in-house with a superconductive fixed point device and a CMN thermometer to reach an accuracy of ± 1 % in the absolute temperature, within the temperature range considered here. All thermometers have then been thoroughly calibrated in field, from 0.2 K to 4 K against a Ge sensor placed in a compensated area of a 18 tesla superconducting magnet and between 2 K and 20 K against a capacitor. The output of this protocol is a quintic bivariable (T and H) spline interpolation sheet, which was used to determine and control the temperature between 0.5 and 20 K up to 18 T with a relative accuracy $\Delta T/T \sim \pm 0.2$ %.

Addenda and test. In order to subtract the heat capacity of the sample mount (chip + a few µg of Apiezon grease used to glue the sample onto the back of the chip), the empty chip (with grease) was measured prior to each sample measurement. This background heat capacity is on the order of $C_{\mathrm{add}} / T \sim 5$ nJ / K^2 at 1 K (3 K) for 1010 (1050) chips, which represents 10 % to 50 % of the heat capacity of the samples.

To benchmark our measurement system and technique, we measured a piece of ultrapure copper, of mass 1 mg, whose heat capacity at low T is comparable to that of our Eu-LSCO and Nd-LSCO samples. In zero magnetic field, the reproducibility between different runs and between different chips shows an absolute accuracy of at least ΔC/C ~ ± 3 % compared to NBS tabulated values, across the range from 0.5 K to 10 K (Supplementary Fig. S3). In magnetic fields up to 18 T, the apparent change $\Delta C / C$ vs H is very smooth and does not exceed 1%.

All factors considered, the absolute accuracy of each of the specific heat runs is estimated to be $\Delta C / C \sim \pm 4\%$, or better. For 0.5 K < T < 5 K, the specific heat is dominated by the electronic contribution and $\Delta C_{el} / C_{el} \sim \Delta C / C$ at T = 0.5 K and 1.0 K. But this error bar increases with temperature, due to the rapid increase in the phonon contribution (and the Schottky term in Nd-LSCO), which makes the electronic term a smaller and smaller fraction of the total signal. The error bars plotted in Fig. 3b and Extended Data Fig. 10a show how this translates into an uncertainty on the absolute value of C_{el} / T for each sample separately, at each temperature.

EXTRACTING THE ELECTRONIC SPECIFIC HEAT

There are three contributions to the specific heat C of Eu-LSCO and Nd-LSCO: from electrons (C_{el}), phonons (C_{ph}) and nuclei (C_{nuclear}). In Nd-LSCO, there is an additional contribution from the magnetic moment on the Nd^{3+} ions (C_{mag}). Because Eu ions are not magnetic, this term is absent in Eu-LSCO. To extract the electronic term of interest here, we proceed as outlined in Extended Data Fig. 6, and described in detail below.

Nuclear Schottky term (C_{nuclear}). The nuclear hyperfine term is a Schottky anomaly peaked at very low temperature. Above the peak, C_{nuclear} dies off rapidly, as $C_{\mathrm{nuclear}} \sim 1/T^2$. In Eu-LSCO and Nd-LSCO, C_{nuclear} is clearly visible in all samples as a rapid upturn below 1 K (Extended Data Fig. 5 and Supplementary Fig. S1). In a field of 8 T, C_{nuclear} becomes negligible above $T \sim 1$ K (Extended Data Fig. 5b, Extended Data Fig. 6a); in 18 T, above ~ 2 K (Extended Data Fig. 5c). By subtracting the raw data for C vs T in Eu-LSCO at $p = 0.16$ from the raw data $C(T)$ at each other doping, we see that the rapid upturn below 1 K is almost entirely removed (Fig. 2b, Supplementary Fig. S1b, Extended Data Fig. 6c), at least down to 0.5 K. (Below $T = 0.5$ K, we do observe that the subtraction is not perfect, reflecting a small difference in the nuclear Schottky anomaly from sample to sample (within ± 20% at 0.3 K), and this is why we report data only for $T = 0.5$ K and above.) This shows that C_{nuclear} is very weakly sample-dependent and doping-dependent. (The nuclear Schottky anomaly is believed to come from the Eu ions (ref. 33), and the Eu content of all our Eu-LSCO samples is kept fixed.)

In summary, to remove C_{nuclear} from the measured C we can work at $T = 1$ K (in 8 T) or at $T = 2$ K in 18 T, and higher temperatures. Below 1 K, we can remove C_{nuclear} reliably down to 0.5 K by subtracting a reference curve, namely $p = 0.16$ in Eu-LSCO and $p = 0.12$ in Nd-LSCO, since C_{nuclear} varies from sample to sample by less than ± 5% at 0.5 K. In Extended Data Fig. 6b, we see the effect of such a subtraction: $(C - C_{\mathrm{nuclear}}) / T$ is constant below 1 K at $p = 0.11$ and $p = 0.16$, while it rises monotonically as $T \rightarrow 0$ at $p = 0.24$. (Note that 8 T is enough to suppress superconductivity in Eu-LSCO down to the lowest temperature for all dopings except $p = 0.21$, where we use 18 T and are limited to $T > 2$ K (Fig. 2b).)

Magnetic Schottky term (C_{mag}). Compared to Eu-LSCO, the specific heat of Nd-LSCO has one additional contribution, C_{mag} , a Schottky peak due to the magnetic moment on the Nd^{3+} ions (Extended Data Fig. 4b). A field moves this magnetic Schottky peak up in temperature, so that C_{mag} becomes very small below 2 K in 8 T and very small below 6 K in 18 T (Extended Data Fig. 5c). We apply the same subtraction procedure as for Eu-LSCO, using our Nd-LSCO sample with $p = 0.12$ as the reference. (The subtraction procedure works well to remove both C_{mag} and C_{nuclear} because the Nd content of all our Nd-LSCO samples is kept fixed.)

At high doping ($p > 0.25$), single crystals are difficult to grow and we have therefore resorted to powder samples of Nd-LSCO, with $p = 0.27$, 0.36 and 0.40. Because these samples are not superconducting, the normal state specific heat can be measured in zero field. Note, however, that the magnetic Schottky term depends on the field direction relative to the c axis of the crystal structure. As a result, we could not use a field to suppress C_{mag} in the powder samples, made of micro-crystallites of all orientations. In Extended Data Fig. 7a, we compare directly the raw data from our powder sample at $p = 0.12$ with the raw data from our single-crystal sample at $p = 0.12$, both at $H = 0$. The two sets of raw data are seen to be in excellent agreement. In the single crystal, we remove C_{mag} by applying a field of 18 T; a fit to $C / T = \gamma + \beta T^2$ below ~ 5 K yields $\gamma = 3.6$ mJ / K^2 mol and $\beta = 0.215$ mJ / K^4 mol (Fig. 2c). In the powder sample, we fit the zero-field raw data to a Schottky anomaly that goes as $C_{mag} \sim 1 / T^2$ (in the range 3 K < T < 7 K). We subtract C_{mag} from the raw powder data and fit the difference to $(C - C_{mag}) / T = \gamma + \beta T^2$ (Extended Data Fig. 7b). The resulting values of γ (4 ± 1 mJ / K^2 mol) and β (0.225 ± 0.015 mJ / K^4 mol) are in good agreement with those quoted above for the $p = 0.12$ single crystal (see Fig. 3b and Extended Data Fig. 6d).

Performing the same fit and subtraction to the zero-field raw powder data at $p = 0.27$, 0.36 and 0.40, reported in Extended Data Fig. 8a, yields curves that are roughly parallel when plotted as $(C - C_{mag}) / T$ vs T^2 (Extended Data Fig. 8b). A fit to $(C - C_{mag}) / T = \gamma + \beta T^2$ yields the values of γ plotted in Fig. 3b (purple dots) and the values of β plotted in Extended Data Fig. 6d (orange dots). The fact that each curve in Extended Data Fig. 8b can be fit to $\gamma + \beta T^2$ shows that the electronic term C_{el} / T is constant in temperature. This is illustrated in Extended Data Fig. 8c, where we subtract the phonon term $C_{ph} = \beta T^3$.

In Extended Data Fig. 8d, we compare the three curves of Extended Data Fig. 8b to raw data on Nd-LSCO (red; from Fig. 2c) and Eu-LSCO (orange; from Fig. 2a) at $p = 0.24$, measured at $H = 18$ T, a field large enough to entirely remove superconductivity. In Eu-LSCO, there is no magnetic Schottky anomaly ($C_{mag} = 0$), and so the orange curve C / T at $p = 0.24$ can be compared directly to the curves $(C - C_{mag}) / T$ vs T^2 at $p = 0.27$, 0.36, and 0.40. We see that the orange curve is not straight, showing a clear upward deviation from linearity at low T. Such a deviation is not seen at $p = 0.36$ and 0.40. At $p = 0.27$, there might be a slight upward deviation, which would not be inconsistent with this doping being close to p^*.

In the Nd-LSCO crystal at $p = 0.24$ (red curve in Extended Data Fig. 8d), a field of 18 T pushes the magnetic Schottky anomaly above ~ 5 K. Below ~ 5 K, the raw curve in Nd-LSCO is essentially identical to the raw curve in Eu-LSCO, confirming that the low-T upward deviation is present in Nd-LSCO also. In conclusion, the log(1/T) behaviour seen at $p = 0.24$ goes away as p increases above p^*.

Phonon term (C_{ph}). At 18 T, superconductivity is completely eliminated from all samples (Extended Data Fig. 4a). At $T > 2$ K, $C_{nuclear}$ is negligible. In Nd-LSCO, C_{mag} is negligible below ~ 6 K. So in the range 2 – 6 K at 18 T, we have $C = C_{el} + C_{ph}$. In

Eu-LSCO at $p = 0.11$ and 0.16, and in Nd-LSCO at $p = 0.12$, the raw data in that T range are well described by $C / T = \gamma + \beta T^2$ (Fig. 2a, Fig. 2c), with very similar values of β (Extended Data Fig. 6d). Alternatively, we can fit the 8 T data from those two samples of Eu-LSCO over the full range from $T = 0.5$ K to 10 K by using $(C - C_{\mathrm{nuclear}}) / T = \gamma + C_{\mathrm{ph}} / T$, where $C_{\mathrm{ph}} / T = \beta T^2 + \delta T^4$, as shown in Extended Data Fig. 6. The two approaches yield very similar values of γ and β (identical within error bars). Fitting single-crystal data away from $p^* = 0.23$, namely Eu-LSCO at $p = 0.08$, 0.11, and 0.16 in 8 T and Nd-LSCO at $p = 0.12$, 0.15, and 0.20 in 18 T, to $(C - C_{\mathrm{nuclear}}) / T = \gamma + \beta T^2 + \delta T^4$ yields the values of β plotted in Extended Data Fig. 6d. For the five powder samples of Nd-LSCO, we fit the zero-field data to $(C - C_{\mathrm{mag}}) / T = \gamma + \beta T^2 + \delta T^4$ (Extended Data Figs. 7b and 8b). In Extended Data Fig. 6d, we see that the doping dependence of β is weak, and in excellent agreement with the very weak doping dependence of the phonon energy, E_{ph}, measured by neutron scattering (Q. Ma *et al.*, to be published), *i.e.* $\beta \sim 1 / E_{\mathrm{ph}}^3$.

Doping dependence of the electronic term (C_{el} vs p). In Extended Data Fig. 6a, we see that C_{nuclear} in 8 T is negligible at $T = 1$ K (and above). In Extended Data Fig. 6b, we see that C_{ph} is negligible at $T = 1$ K (and below). Therefore the raw data at $T = 1$ K and $H = 8$ T, in Eu-LSCO, directly give the electronic specific heat at 1 K, *i.e.* $C_{\mathrm{el}} = C$ to a very good approximation (except at $p = 0.21$, where 8 T is not enough to fully suppress superconductivity). The huge rise in C from $p = 0.11$ to $p = 0.24$ (Fig. 3a) is therefore entirely due to C_{el}.

At high doping, beyond p^*, the Nd-LSCO powder data show a clear decrease in γ as p increases (Extended Data Fig. 8b). The result is therefore an unambiguous peak, at $p = p^*$, in C_{el} vs p in the $T = 0$ limit (Fig. 3a). This is the first key signature of a QCP.

Temperature dependence of the electronic term (C_{el} vs T). Extended Data Fig. 6 shows that C_{el} / T at $p = 0.16$ is constant as a function of T, all T dependence being due to C_{nuclear} / T and C_{ph} / T. The same is true at $p = 0.11$. At $p = 0.24$, however, there is an additional T dependence not due to C_{nuclear} or C_{ph}, which comes from $C_{\mathrm{el}}(T)$. The simplest way to reveal this T dependence of $C_{\mathrm{el}}(T)$ is to subtract the raw curve at $p = 0.16$ from the raw curve at $p = 0.24$, as done in Fig. 2b. Or, equivalently, subtract the fit to $(C - C_{\mathrm{nuclear}} - C_{\mathrm{ph}}) / T$ performed on the $p = 0.16$ data, as done in Extended Data Fig. 6c. Both approaches yield a clean $\log(1/T)$ dependence for C_{el} / T at $p = 0.24$, from 0.5 K to 10 K (see dotted line in Extended Data Fig. 6c).

These approaches assume that C_{nuclear} is the same in the two samples, which is true to better than 5%, and also that C_{ph} at $p = 0.24$ is the same as C_{ph} at $p = 0.16$, which is true to better than 4%, as established by the neutron data : E_{ph} changes from 14.6 meV at p = 0.12 to 14.8 meV at p = 0.24. In other words, within error bars, we find that C_{el} / $T \sim \log(1/T)$ up to at least 10 K. This is the second key signature of a QCP.

In Extended Data Fig. 10a, we plot the value of C_{el} / T at T = 0.5 K, 2 K and 10 K, obtained using the first procedure of simply subtracting two raw curves, requiring no fitting at all. As we have just shown, the values of C_{el} / T obtained in this way are accurate and reliable, within the error bars.

The fact that C_{el} /T keeps increasing as $T \rightarrow 0$ at p = 0.24 is confirmed directly by looking at ΔC / T_c , the jump in C_{el} /T at T_c , the two being linked by entropy balance. In Extended Data Fig. 3, we see that ΔC / T_c increases by a factor 10 in going from p = 0.11 to p = 0.24, in tandem with the increase in C_{el} /T at T = 0.5 K (Fig. 3b) – separate evidence from raw data (with no analysis or subtraction) that C_{el} /T at p = 0.24 must increase below 10 K.

In summary, the high level of quantitative consistency we find between the values of C_{el} /T obtained in our 5 crystals of Eu-LSCO and those obtained in our 7 crystals of Nd-LSCO (Fig. 3b) is a strong validation of both the experimental technique and the data analysis. It confirms that the electronic specific heat $C_{el}(T)$ we report is reproducible and accurate (within the quoted error bars). Furthermore, the excellent agreement between the values of $C_{el}(T)$ plotted in Fig. 3b and the raw values of $C(T)$ at T = 1 K and 2 K plotted in Fig. 3a confirms the fidelity of our analysis, as does the parallel growth observed in ΔC / T_c and C_{el} /T (Fig. 3b).

VAN HOVE SINGULARITY

In hole-doped cuprates, the large Fermi surface in the overdoped regime undergoes a change of topology from hole-like to electron-like at some material-dependent critical doping p_{vHs} . According to ARPES, this change of topology occurs between p = 0.15 and p = 0.22 in LSCO (ref. 34) and between p = 0.20 and p = 0.24 in Nd-LSCO (ref. 14), *i.e.* close to p^* in both cases (Extended Data Fig. 1; ref. 35). If the Fermi surface were strictly two-dimensional, this would, in the clean limit, lead to a van Hove singularity in the density of states, producing a cusp in C_{el} / T vs p at p_{vHs} and a $\log(1/T)$ dependence of C_{el} / T as $T \rightarrow 0$, analogous to the behavior we report in Eu-LSCO and Nd-LSCO.

However, the change of Fermi-surface topology at $p_{vHs} \sim p^*$ cannot in fact be responsible for that behavior, for two reasons: because of the significant 3D character of the Fermi surface in Nd-LSCO (and Eu-LSCO), and because of the significant level of disorder in our samples. Each of these two mechanisms broadens the van Hove singularity, removes the cusp vs p and cuts off the log(1/T) divergence at low T.

To be quantitative, we have calculated the specific heat of Nd-LSCO associated with its known band structure, using the following one-band model (ref. 36):

$$\xi_{\mathbf{k}} = -\mu - 2t\left(\cos(k_x a) + \cos(k_y b)\right) - 4t' \cos(k_x a)\cos(k_y b) - 2t''\left(\cos(2k_x a)\cos(2k_y b)\right)$$
$$- 2t_z \cos(k_z c/2)\left[\cos(k_x a) - \cos(k_y b)\right]^2 \cos(k_x a/2)\cos(k_y b/2)$$

with t = 0.189 meV, t' = – 0.17t, t'' = 0.05t. Those parameters agree with the experimental band structure measured by ARPES (ref. 37), and are such that the vHs is located at p = 0.23. The 3D character is controlled by the interlayer hopping parameter t_z. The doping is adjusted by tuning the chemical potential μ.

The temperature-dependent specific heat is given by[38] :

$$C_{el}(T) = \int_{-\infty}^{\infty} d\epsilon \frac{\partial f(\epsilon)}{\partial T} \epsilon N(\epsilon)$$

with:

$$N(\epsilon) = \frac{1}{V}\sum_{\mathbf{k}} \frac{1}{\pi} \frac{\hbar/2\tau}{(\epsilon - \xi_{\mathbf{k}})^2 + (\hbar/2\tau)^2}$$

where $f(\varepsilon)$ is the Fermi-Dirac function, $N(\varepsilon)$ is the density of state, and τ is the quasiparticle lifetime.

The calculated specific heat is shown in Extended Data Fig. 9 (blue), as a function of doping (at $T \rightarrow 0$) on the left and as a function of temperature (at $p = p_{vHs}$) on the right. In the top panels, we show the clean-limit 2D result, with $\hbar$ / τ = 0 and t_z = 0. In the middle panels, we show the effect of disorder, with $\hbar$ / τ = t / 25, the value needed to produce the measured residual resistivity of our Nd-LSCO and Eu-LSCO samples at p = 0.24, namely ρ_0 ~ 30 μΩ cm (Extended Data Fig. 2). In the lower panels, we further add the effect of 3D dispersion, with t_z = 0.13t, the value needed to produce the measured anisotropy of Nd-LSCO at p = 0.24, namely ρ_c / ρ_a ~ 250 (ref. 39).

Direct comparison with our data shows that band structure effects associated with p_{vHs} in Nd-LSCO do produce a broad background bump in C_{el} vs p, but they cannot account for the large and sharp peak we observe in C_{el} / T at T = 0.5 K (Extended Data Fig. 9). Moreover, the fact that we see C_{el} / T ~ log(1/T) persisting down to 0.5 K at p = p* completely excludes a van Hove mechanism, which yields a constant C_{el} / T when $k_B T < \hbar / \tau$ or when $k_B T < t_z$, *i.e.* below ~ 20 K in our samples (Extended Data Fig. 9).

Recent calculations of C_{el} / T vs p at $T = 0$ using the real 3D electronic structure measured by ARPES in LSCO and Eu-LSCO (ref. 40) yield curves that are essentially identical, quantitatively, with our own curves in Extended Data Fig. 9, showing again that the vHs cannot account for the large peak observed in Nd-LSCO, Eu-LSCO or LSCO. Even when the authors of ref. 40 assume no disorder ($1 / \tau = 0$), they find that the 3D dispersion alone limits the increase in C_{el} / T from $p = 0.40$ to $p = 0.24$ to no more than a factor 2, whereas our data show a 4-fold increase (Fig. 3b).

Note that strong disorder does not alter the $\log(1/T)$ dependence of C_{el} /T coming from a QCP, as demonstrated by its persistence down to ~ 20 mK in samples of $CeCu_{5.9}Au_{0.1}$ (ref. 6) that have a residual resistivity ρ_0 larger than that of our own samples at $p = 0.24$ (Extended Data Fig. 2).

Data availability. The data that support the plots within this paper and other findings of this study are available from the corresponding author upon reasonable request.

EXTENDED DATA FIGURE CAPTIONS

Extended Data Fig. 1 | Temperature-doping phase diagram.

Temperature-doping phase diagram of LSCO (black), Nd-LSCO (red) and Eu-LSCO (green), showing the boundary of the phase of long-range commensurate antiferromagnetic order (T_N , brown line), the pseudogap temperature T^* (blue line) and the superconducting transition temperature T_c of LSCO (grey line) and Nd-LSCO (pink line). T^* is detected in two transport properties : resistivity (T_ρ , circles) and the Nernst effect (T_ν , squares). The open triangles show T^* detected by ARPES as the temperature below which the anti-nodal pseudogap opens, in LSCO (black) and Nd-LSCO (red). We see that $T_\nu \simeq T_\rho \simeq T^*$, within error bars. The pseudogap phase ends at a critical doping $p^* = 0.18 \pm 0.01$ in LSCO (black diamond) and $p^* = 0.23 \pm 0.01$ in Nd-LSCO (red diamond). Figure adapted from ref. 35.

Extended Data Fig. 2 | Characterization of our samples of Eu-LSCO and Nd-LSCO.

a) T_c vs p for our Eu-LSCO samples. T_c is defined as the onset of the drop in the magnetization upon cooling. **b)** Same for our Nd-LSCO samples. **c)** ρ vs T in our

Eu-LSCO samples with $p = 0.21$ (red) and $p = 0.24$ (blue), at $H = 0$ and $H = 33$ T (short section below 40 K). **d)** Same for our Nd-LSCO samples with $p = 0.22$ (red) and $p = 0.24$ (blue) (ref. 2). The approximately linear $\rho(T)$ as $T \to 0$ at $p = 0.24$ (blue) shows that 0.24 is close to the critical point $p^* \sim 0.23$ in both materials. The large upturn in $\rho(T)$ as $T \to 0$ at $p = 0.21$ and $p = 0.22$ (red) shows that the pseudogap has opened in both materials (at $p < 0.23$).

Extended Data Fig. 3 | Specific heat jump at T_c in Eu-LSCO.

a) C / T vs T in our Eu-LSCO sample with $p = 0.24$, at $H = 0$ (red) and $H = 8$ T (blue). *Inset*: Difference between the two curves in the main panel (red). This is the difference between the superconducting-state C / T and the normal-state C / T. It reveals the jump at T_c, whose peak value, $\Delta C / T_c$, is defined as drawn. The black curve is the magnetization of that sample. At $p = 0.24$, the bulk $T_c = 10.5 \pm 0.5$ K (dashed line). **b)** As in panel a, for our sample with $p = 0.21$, at $H = 0$ (red) and $H = 18$ T (blue). At $p = 0.21$, the bulk $T_c = 14.5 \pm 0.5$ K. **c)** As in panel a, for our sample with $p = 0.16$, at $H = 0$ (red) and $H = 18$ T (blue). At $p = 0.16$, the bulk $T_c = 11.5 \pm 0.5$ K. **d)** As in panel a, for our sample with $p = 0.11$, at $H = 0$ (red) and $H = 8$ T (blue). At $p = 0.11$, the bulk $T_c = 5.0 \pm 0.5$ K. **e)** Plot of $\Delta C / T_c$ vs C_{el} / T at $T = 0.5$ K, the latter being obtained from Fig. 3b (red squares). The error bar on $\Delta C / T_c$ comes mostly from the uncertainty on defining the baseline above T_c. The dashed line is a linear fit through the first three data points. The 10-fold increase in $\Delta C / T_c$ from $p = 0.11$ to $p = 0.24$ is independent evidence of a similar increase in C_{el} / T.

Extended Data Fig. 4 | Specific heat as a function of magnetic field.

a) C / T vs H in our Eu-LSCO samples with $p = 0.21$ (orange) and $p = 0.24$ (red), at $T = 2$ K. The upper critical field above which there is no remaining superconductivity is $H_{c2} = 15$ T at $p = 0.21$ and $H_{c2} = 9$ T at $p = 0.24$. Note that for $p = 0.24$, C / T has reached 99 % of its normal state value by 8 T. **b)** C / T vs H in our Nd-LSCO sample with $p = 0.23$, at $T = 2$ K, in a semi-log plot. The dashed line shows the expected field dependence of the Schottky contribution associated with Nd ions (C_{mag}, dashed line). The data are independent of field above $H \sim 9$ T. Dotted lines are horizontal.

Extended Data Fig. 5 | Specific heat of Eu-LSCO and Nd-LSCO at *H* = 8 T.

a) Specific heat of the four Eu-LSCO samples of Fig. 2a measured in a field H = 8 T, down to 0.4 K. The rapid rise below 1 K is a nuclear Schottky anomaly (C_{nuclear}). **b)** Difference between the measured C / T of panel a and a constant term γ, plotted for each doping as a function of temperature, on a log-log plot (γ = 2.8 and 4.2 mJ /K^2 mol, at p = 0.11 and 0.16, respectively). The line marked T^2 shows that the data at p = 0.11 and p = 0.16 obey $\Delta C = \beta T^3$ in the range from 1.5 K to ~ 5 K. The line marked T^{-3} shows that the data at p = 0.11 and p = 0.16 obey $\Delta C \sim T^{-2}$ below 1 K, as expected for the upper tail of a Schottky anomaly. The ΔC curve at p = 0.16, $\Delta C(p{=}0.16; T)$, therefore constitutes the non-electronic, and weakly doping-dependent, background for $C(T)$ in Eu-LSCO, made of phonon and Schottky contributions. **c)** Specific heat of our Nd-LSCO crystal with p = 0.12, plotted as C / T vs T at three different fields, as indicated. At H = 0 (green), we see the large Schottky anomaly associated with Nd ions, varying as $C_{\mathrm{mag}} \sim T^{-2}$ at low T. At H = 8 T (red), it is pushed up above 2 K; at H = 18 T (blue), above 5 K. The line is a fit of the 18 T data to $\gamma + \beta T^2$ below 5 K. **d)** Specific heat of the four Nd-LSCO samples of Fig. 2c, plotted as C / T vs T. Below the vertical dashed line, we show low-temperature data taken at H = 8 T on three of these same samples. (See Supplementary Fig. S1 for the complete set of dopings, and Extended Data Fig. 6 for further analysis and discussion.)

Extended Data Fig. 6 | Analysis of specific heat data and doping dependence of β.

a) Raw data for Eu-LSCO at p = 0.11 (blue), 0.16 (green) and 0.24 (red), plotted as C / T vs log$T$. The width of the pale band tracking each curve is the uncertainty on the absolute measurement of C (± 4%). The solid green line is a fit to $C_{\mathrm{nuclear}} \sim T^{-2}$ for the p = 0.16 data. **b)** Same three curves as in panel a, from which the same Schottky anomaly, C_{nuclear} / T, the green line in panel a, has been subtracted. The straight dotted lines show that $(C - C_{\mathrm{nuclear}})$ / T is flat as $T \rightarrow 0$ for p = 0.11 and 0.16, while it rises as log(1/T) for p = 0.24. The solid green line is a fit of the green curve at p = 0.16 to $(C - C_{\mathrm{nuclear}})/T = \gamma + C_{\mathrm{ph}} / T$ up to 10 K, where $C_{\mathrm{ph}} / T = \beta T^2 + \delta T^4$ is the phonon contribution. **c)** Same three curves as in panel b, from which the same phonon contribution C_{ph} / T, the green line in panel b, has been subtracted. We see that within error bars the resulting C_{el} / T is constant up to 10 K for $p = 0.11$ (blue) and 0.16 (green), while it varies as $\log(1/T)$ up to 10 K for $p = 0.24$ (red). The dotted lines are a linear fit to the data. **d)** Doping dependence of the phonon specific heat parameter β , in $C_{ph} / T = \beta T^2 + \delta T^4$, obtained from a fit to $(C - C_{nuclear}) / T = \gamma + C_{ph} / T$ up to 10 K, for Eu-LSCO crystals (dark blue squares) and Nd-LSCO crystals (red dots). For Nd-LSCO powders (orange dots), the values are obtained from Extended Data Figs. 7 and 8. The black diamonds are $1 / E_{ph}{}^3$ (right axis), where E_{ph} is the phonon energy (top of the acoustic branch) measured by neutron scattering on three Nd-LSCO single crystals: E_{ph} = 14.6, 14.7, and 14.8 meV at $p = 0.12$, 0.19, and 0.24, respectively (Q. Ma *et al.*, to be published). We see that E_{ph} varies very little with doping, and $\beta \sim 1 / E_{ph}{}^3$, justifying our assumption that $C_{ph}(T)$ does not change appreciably between $p = 0.11$ and $p = 0.25$.

Extended Data Fig. 7 |Specific heat of our polycrystalline samples at *p* = 0.07, 0.12.

a) C / T vs T for Nd-LSCO $p = 0.12$, comparing raw data on crystal and powder, as indicated. The solid red line is a fit to the crystal data, consisting of the sum of three contributions, plotted below: electrons (dash-dotted), phonons (dashed) and Schottky ($C_{mag} \sim T^{-2}$, dotted). **b)** Specific heat data for our powders with $p = 0.07$ and 0.12, at $H = 0$, from which the Schottky term (C_{mag}) has been subtracted, plotted as $(C(H = 0) - C_{mag}) / T$ vs T^2. The dashed lines are linear fits to the data ($\gamma + \beta T^2$). For $p = 0.12$, the fit yields $\gamma \sim 4.0$ mJ / K^2 mol, in reasonable agreement with the value obtained by applying 18 T to suppress the Schottky anomaly in our Nd-LSCO crystal with $p = 0.12$ (Fig. 2c), namely $\gamma = 3.6 \pm 0.5$ mJ / K^2 mol (Fig. 3b). For the two powder samples, the γ values are plotted in Fig. 3b (purple dots) and the β values are plotted in Extended Data Fig. 6d (orange dots). The value of $(C(H = 0) - C_{mag}) / T$ extrapolated at $T = 2$ K is plotted in Fig. 3a (open red circles).

Extended Data Fig. 8 | Specific heat of our polycrystalline samples at *p* = 0.27, 0.36, 0.40.

a) Raw specific heat data for our powders with $p = 0.27$, 0.36 and 0.40, at $H = 0$. **b)** Data in a) from which the magnetic Schottky term ($C_{mag} = A/T^2$) has been subtracted, plotted as $(C - C_{mag}) / T$ vs T^2. The dotted lines are linear fits to the data ($\gamma + \beta T^2$).

For the three powder samples, the γ values are plotted in Fig. 3b (purple dots) and the β values are plotted in Extended Data Fig. 6d (orange dots). The value of $(C(H=0) - C_{mag}) / T$ extrapolated at $T = 2$ K is plotted in Fig. 3a (open red circles). **c)** Data in b) from which the phonon term ($C_{ph} = \beta T^3$) has been subtracted, plotted as $(C - C_{mag} - C_{ph}) / T$ vs T^2. All three curves are seen to be constant. **d)** Data in b), compared to raw single-crystal data at $p = 0.24$ for Eu-LSCO (orange) and Nd-LSCO (red), taken at $H = 18$ T. (The two raw curves agree beautifully at $T < 5$ K, where C_{mag} in Nd-LSCO is negligible (Extended Data Fig. 5c).) The upper dotted line is a linear guide to the eye showing that the Eu-LSCO curve deviates from linearity at low temperature, unlike the curves at $p = 0.27$, 0.36 and 0.40.

Extended Data Fig. 9 | Calculated specific heat from the Nd-LSCO band structure.

Comparison of the measured specific heat of Nd-LSCO (red; Fig. 3b) and the specific heat calculated for the band structure of Nd-LSCO (blue; see Methods), with the van Hove point p_{vHs} set to be at p^*. The calculations include the 3D dispersion in the Fermi surface (along k_z) and the disorder scattering, both consistent with the measured properties of our Nd-LSCO samples, namely their *a*-*c* anisotropy in the conductivity and their residual resistivity (see Methods). We see that while the vHs can give rise to a cusp-like peak at p_{vHs} (top left panel) and a $\log(1/T)$ dependence of C/T at p_{vHs} in a perfectly 2D system with no disorder (lower left panel), these features inevitably disappear when the considerable 3D dispersion of the real material and the high disorder of the real samples are included (right panels). The calculations only quantify what is naturally expected: the rise in specific heat due to the vHs is cut off when $k_B T < \hbar \Gamma$, where Γ is the scattering rate, or when $k_B T < t_z$, where t_z is the *c*-axis hopping parameter. The fact that we see C / T continuing to increase down to 0.5 K (lower right panel) excludes the vHs as the underlying mechanism.

Extended Data Fig. 10 | Comparing with data on non-superconducting LSCO.

a) Normal-state electronic specific heat C_{el} of Eu-LSCO (squares; from Fig. 2b) and Nd-LSCO (circles; from Fig. 2d), at $T = 0.5$ K (red), 2 K (blue) and 10 K (green), plotted as C_{el} / T vs p. (At $p = 0.08$, 0.11 and 0.16, the red and green squares are split apart slightly so they can both be seen.) Open symbols are extrapolated values (dashed lines in Fig. 2b and Fig. 2d). Data on Nd-LSCO at p = 0.07, 0.12, 0.27, 0.36 and 0.40 (purple) are γ values obtained on polycrystalline samples, as described in Extended Data Figs. 7 and 8. Error bars are explained in the Methods. We also include γ for non-superconducting LSCO from published work (diamonds), obtained by extrapolating $C / T = \gamma + \beta T^2$ to $T = 0$ from data below 10 K ($p < 0.06$ (ref. 32); $p = 0.33$ (ref. 13)). The vertical dashed line marks the pseudogap critical point p* in Nd-LSCO (Extended Data Fig. 1). All solid lines are a guide to the eye. **b)** Comparison of C_{el} / T vs p in our samples of Eu-LSCO and Nd-LSCO at T = 10 K (green squares and circles, panel a) with published data on non-superconducting LSCO (diamonds). Open diamonds are γ measured in single crystals of LSCO at dopings where there is no superconductivity (p = 0.33 (ref. 13); p < 0.05 (ref. 32); remainder (ref. 17)). Full diamonds are data from powders made non-superconducting by Zn substitution (ref. 17); γ values are obtained from fits to $C / T = \gamma + \beta T^2$ between ~ 4 K and ~ 8 K. We see that these early data on LSCO are quantitatively consistent with our data on Eu-LSCO and Nd-LSCO, apart from a downward shift in the position of the peak, consistent with a lower p* in LSCO (Extended Data Fig. 1). Lines are a guide to the eye.

---

[1] Taillefer, L. Scattering and pairing in cuprate superconductors. *Annu. Rev. Condens. Matter Phys.* **1**, 51-70 (2010).

[2] Collignon, C. *et al*. Fermi-surface transformation across the pseudogap critical point of the cuprate superconductor $La_{1.6-x}Nd_{0.4}Sr_xCuO_4$. *Phys. Rev. B.* **95**, 224517 (2017).

[3] Löhneysen, H. v. *et al.* Fermi-liquid instabilities at magnetic quantum phase transitions. *Rev. Mod. Phys.* **79**, 1015 (2007).

[4] Monthoux, P., Pines, D. & Lonzarich, G. G. Superconductivity without phonons. *Nature* **450**, 1177-1183 (2007).

[5] Shibauchi, T., Carrington, A. & Matsuda, Y. A quantum critical point lying beneath the superconducting dome in iron pnictides. *Annu. Rev. Condens. Matter Phys*. **5**, 113-135 (2014).

[6] Löhneysen, H. v. *et al.* Non-Fermi-liquid behavior in a heavy-fermion alloy at a magnetic instability. *Phys. Rev. Lett.* **72**, 3262-3265 (1994).

[7] Walmsley, P. *et al.* Quasiparticle mass enhancement close to the quantum critical point in $BaFe_2(As_{1-x}P_x)_2$. *Phys. Rev. Lett.* **110**, 257002 (2013).

[8] Doiron-Leyraud, N. *et al*. Correlation between linear resistivity and T_c in the Bechgaard salts and the pnictide superconductor $Ba(Fe_{1-x}Co_x)_2As_2$. *Phys. Rev. B.* **80**, 214531 (2009).

[9] Ramshaw, B. J. *et al.* Quasiparticle mass enhancement approaching optimal doping in a high-T_c superconductor. *Science* **348**, 317-320 (2015).

[10] Kačmarčík, J. *et al.* Unusual interplay between superconductivity and field-induced charge order in $YBa_2Cu_3O_y$. *Phys. Rev. Lett.* **121**, 167002 (2018).

[11] Loram, J. W. *et al.* Electronic specific heat of $YBa_2Cu_3O_{6+x}$ from 1.8 to 300 K. *Phys. Rev. Lett.* **71**, 1740-1743 (1993).

[12] Loram, J. W. *et al.* Specific heat evidence on the normal state pseudogap. *J. Phys. Chem. Solids* **59**, 2091-2094 (1998).

[13] Nakamae, S. *et al*. Electronic ground state of heavily overdoped nonsuperconducting $La_{2-x}Sr_xCuO_4$. *Phys. Rev. B.* **68**, 100502R (2003).

[14] Matt, C. E. *et al*. Electron scattering, charge order, and pseudogap physics in $La_{1.6-x}Nd_{0.4}Sr_xCuO_4$: An angle-resolved photoemission spectroscopy study. *Phys. Rev. B* **92**, 134524 (2015).

[15] Trovarelli, O. *et al.* $YbRh_2Si_2$: pronounced non-Fermi-liquid effects above a low-lying magnetic phase transition. *Phys. Rev. Lett.* **85**, 626-629 (2000).

[16] Bianchi, A. *et al.* Avoided antiferromagnetic order and quantum critical point in $CeCoIn_5$. *Phys. Rev. Lett.* **91**, 257001 (2003).

[17] Momono, N. *et al.* Low-temperature electronic specific heat of $La_{2-x}Sr_xCuO_4$ and $La_{2-x}Sr_xCu_{1-y}Zn_yO_4$. Evidence for a *d*-wave superconductor. *Physica C* **233**, 395-401 (1994).

[18] Wade, J. M. *et al.* Electronic specific heat of $Tl_2Ba_2CuO_{6+\delta}$ from 2 K to 300 K for $0 < \delta < 0.1$. *J. Supercon.* **7**, 261-264 (1994).

[19] Bangura, A. F. *et al.* Fermi surface and electronic homogeneity of the overdoped cuprate superconductor $Tl_2Ba_2CuO_{6+\delta}$ as revealed by quantum oscillations. *Phys. Rev. B* **82**, 140501 (2010).

[20] Loram, J. W. *et al.* Evidence on the pseudogap and condensate from the electronic specific heat. *J. Phys. Chem. Solids* **62**, 59-64 (2001).

[21] Loret, B. *et al.* Raman and ARPES combined study on the connection between the existence of the pseudogap and the topology of the Fermi surface in $Bi_2Sr_2CaCu_2O_{8+\delta}$. *Phys. Rev. B* **97**, 174521 (2018).

[22] Chan, M. K. *et al.* Single reconstructed Fermi surface pocket in an underdoped single-layer cuprate superconductor. *Nat. Commun.* **7**, 12244 (2016).

[23] Grissonnanche, G. *et al.* Direct measurement of the upper critical field in cuprate superconductors. *Nat. Commun.* **5**, 3280 (2014).

[24] E. M. Motoyama *et al.* Spin correlations in the electron-doped high-transition-temperature superconductor $Nd_{2-x}Ce_xCuO_{4\pm\delta}$. *Nature* **445**, 186 (2007).

[25] Dagan, Y. *et al.* Evidence for a quantum phase transition in $Pr_{2-x}Ce_xCuO_{4-\delta}$ from transport measurements. *Phys. Rev. Lett.* **92**, 167001 (2004).

[26] Storey, J. G. *et al*. Pseudogap ground state in high-temperature superconductors. *Phys. Rev. B* **78**, 140506(R) (2008).

[27] Tranquada, J. M. *et al*. Coexistence of, and competition between, superconductivity and charge-stripe order in $La_{1.62-x}Nd_{0.4}Sr_xCuO_4$. *Phys. Rev. Lett.* **78**, 338 (1997).

[28] Nachumi, B. *et al.* Muon spin relaxation study of the stripe phase order in $La_{1.6-x}Nd_{0.4}Sr_xCuO_4$ and related 214 cuprates. *Phys. Rev. Lett.* **58**, 8760 (1998).

[29] Chatterjee, S. & Sachdev, S. Insulators and metals with topological order and discrete symmetry breaking. *Phys. Rev. B* **95**, 205133 (2017).

[30] Nie, L., Tarjus, G. & Kivelson, S. A. Quenched disorder and vestigial nematicity in the pseudogap regime of the cuprates. *PNAS* **111**, 7980-7985 (2014).

[31] Varma, C. M. Quantum-critical fluctuations in 2D metals: strange metals and superconductivity in antiferromagnets and in cuprates. *Rep. Prog. Phys.* **79**, 082501 (2016).

[32] Komiya, S. & Tsukada, I. Doping evolution of the electronic specific heat coefficient in slightly-doped $La_{2-x}Sr_xCuO_4$ single crystals. *J. Phys. Conference Series* **150**, 052118 (2009).

[33] Ghamaty, S. *et al*. Low temperature specific heat of Ln_2CuO_4 (Ln = Pr, Nd, Sm, Eu and Gd) and $Nd_{1.85}M_{0.15}CuO_{4-y}$ (M = Ce and Th). *Physica C* **160**, 217-222 (1989).

[34] Yoshida, T. *et al*. Systematic doping evolution of the underlying Fermi surface of $La_{2-x}Sr_xCuO_4$. *Phys. Rev. B* **74**, 224510 (2006).

[35] Cyr-Choinière, O. *et al.* Pseudogap temperature T^* of cuprate superconductors from the Nernst effect. *Phys. Rev. B* **97**, 064502 (2018).

[36] Markiewicz, R. S. *et al*. One-band tight-binding model parametrization of the high-T_c cuprates including the effect of k_z dispersion. *Phys. Rev. B* **72**, 054519 (2005).

[37] Matt, C. E. *et al*. Direct observation of orbital hybridisation in a cuprate superconductor. *Nat. Commun.* **9**, 972 (2018).

[38] Verret, S. *et al.* Phenomenological theories of the low-temperature pseudogap: Hall number, specific heat, and Seebeck coefficient. *Phys. Rev. B* **96**, 125139 (2017).

[39] Daou, R. *et al.* Linear temperature dependence of resistivity and change in the Fermi surface at the pseudogap critical point of a high-T_c superconductor. *Nat. Phys*. **5**, 31-34 (2009).

[40] Horio, M. *et al*. Three-dimensional Fermi surface of overdoped La-based cuprates. *Phys. Rev. Lett.* **121**, 077004 (2018).

Main Figure 1

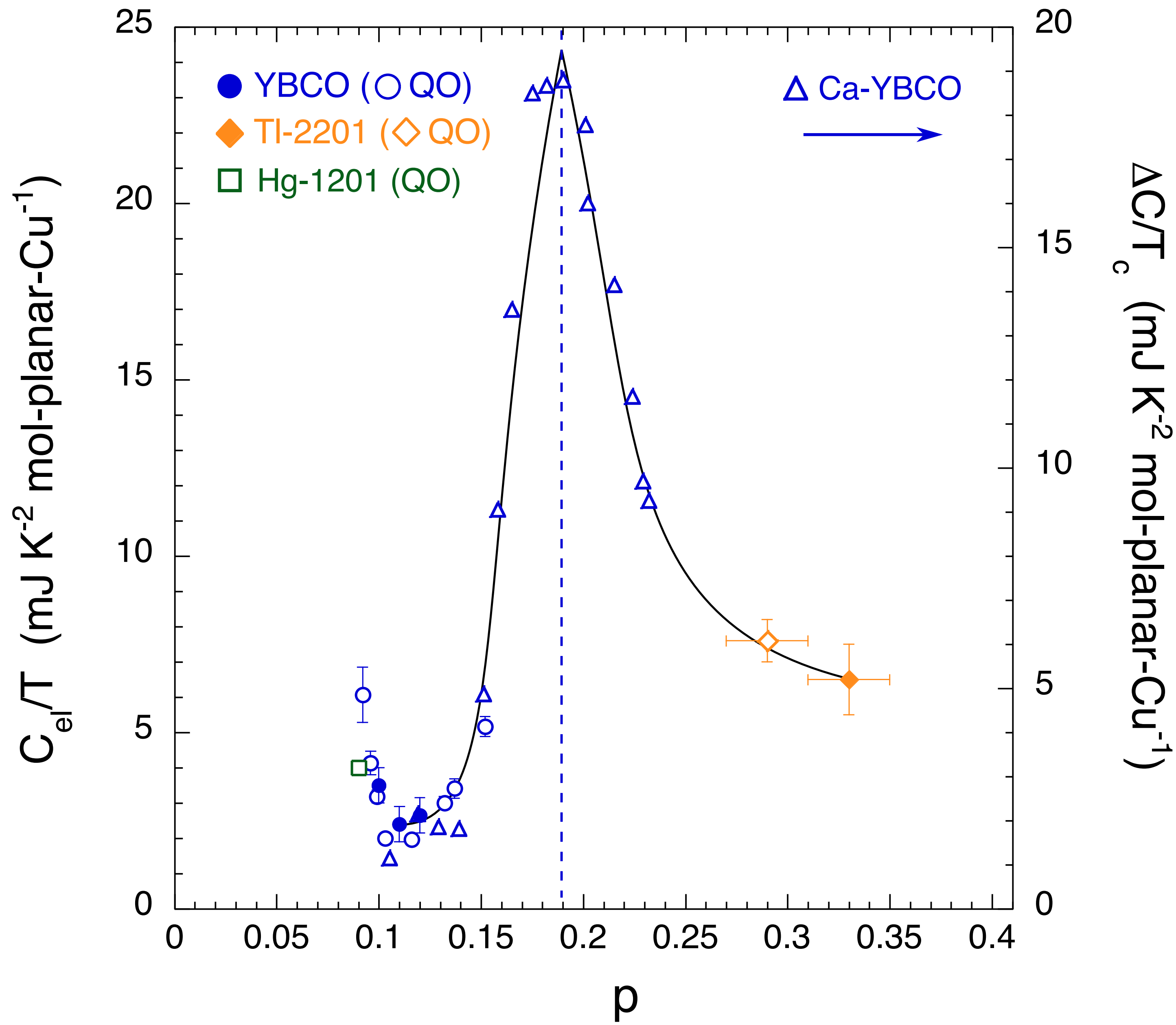

Main Figure 2

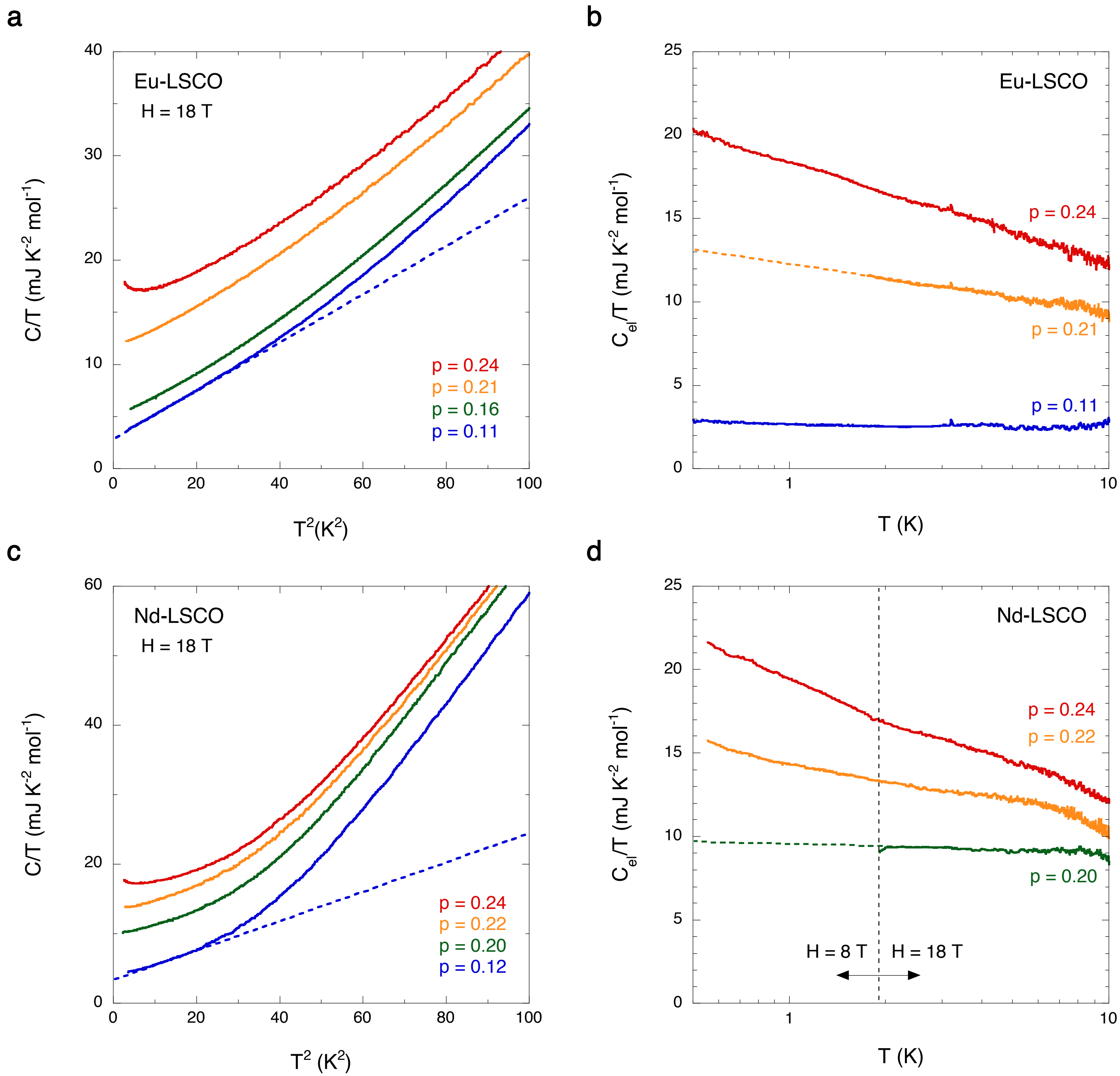

Main Figure 3

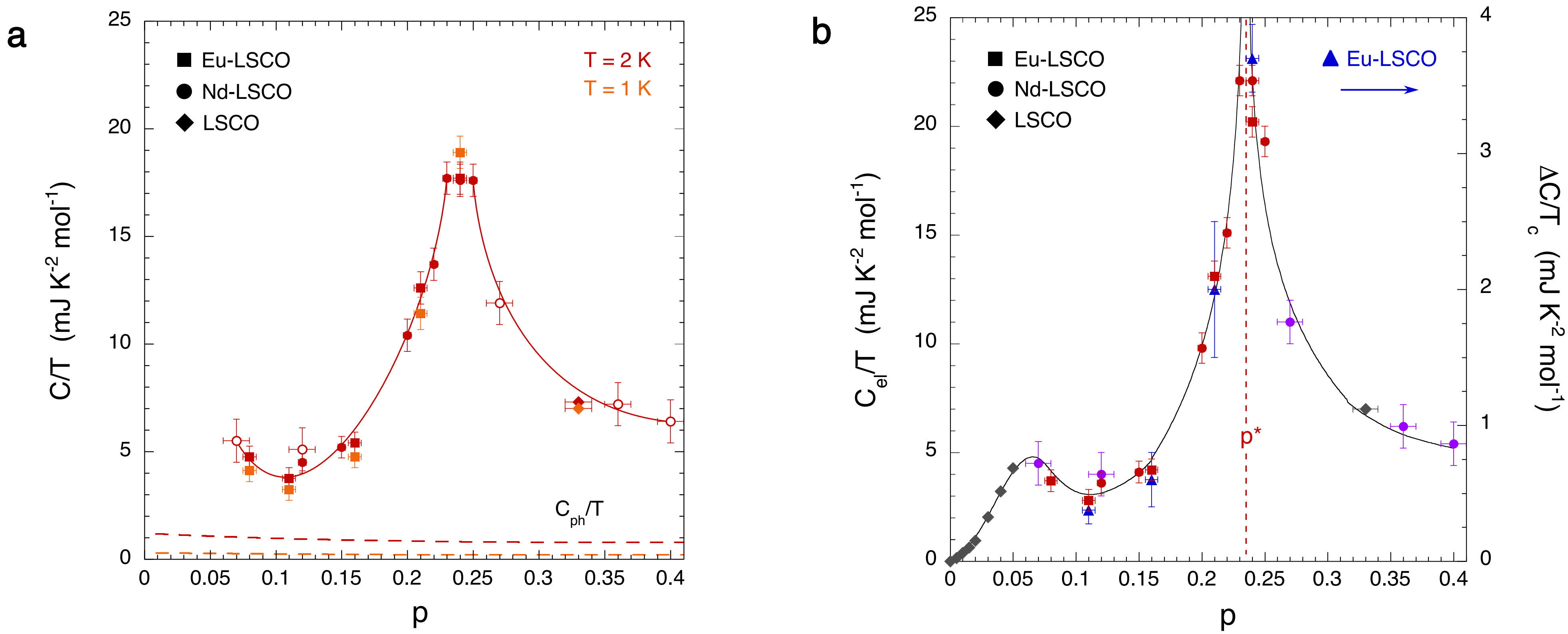

Extended Data Figure 1

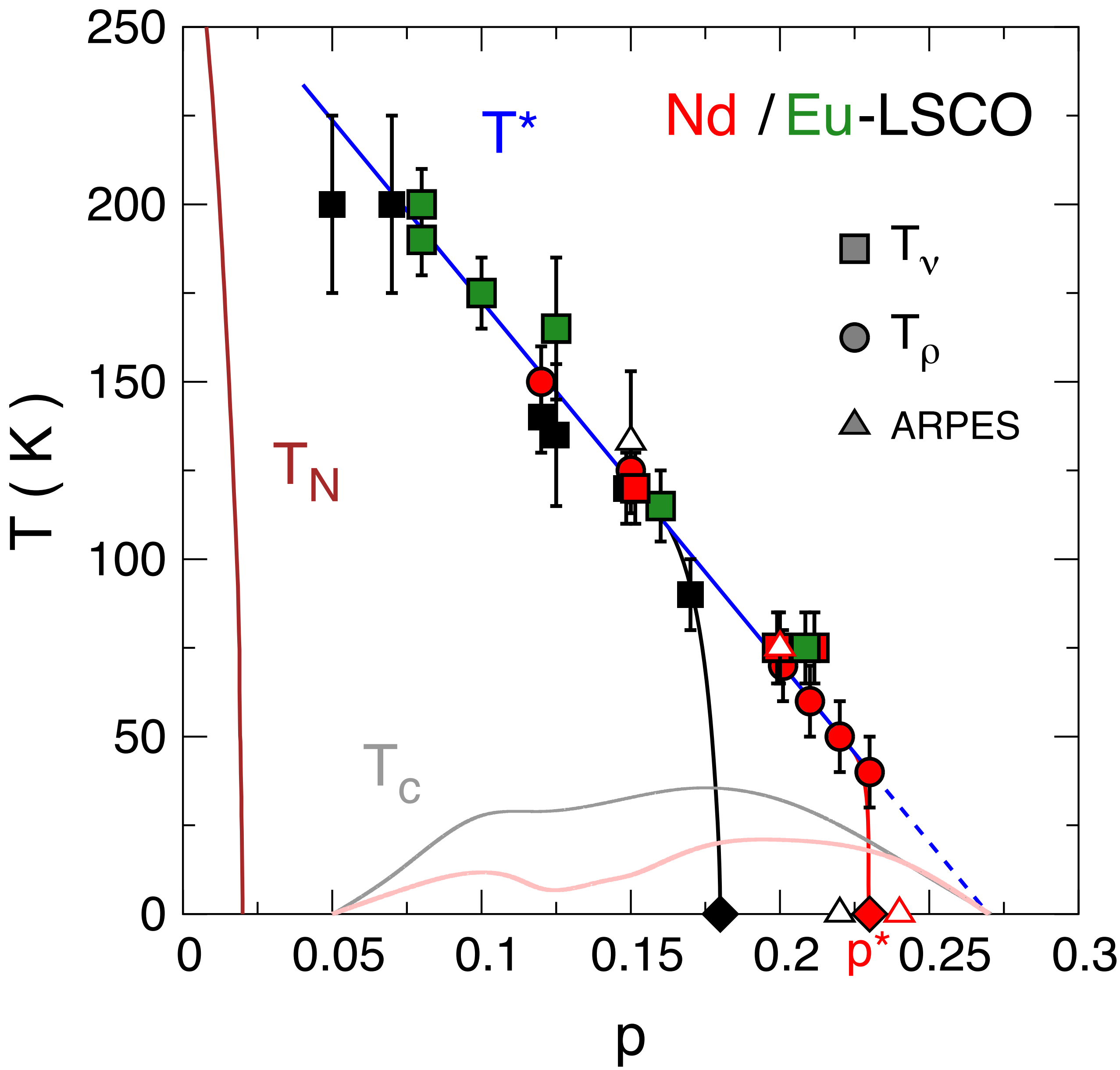

Extended Data Figure 2

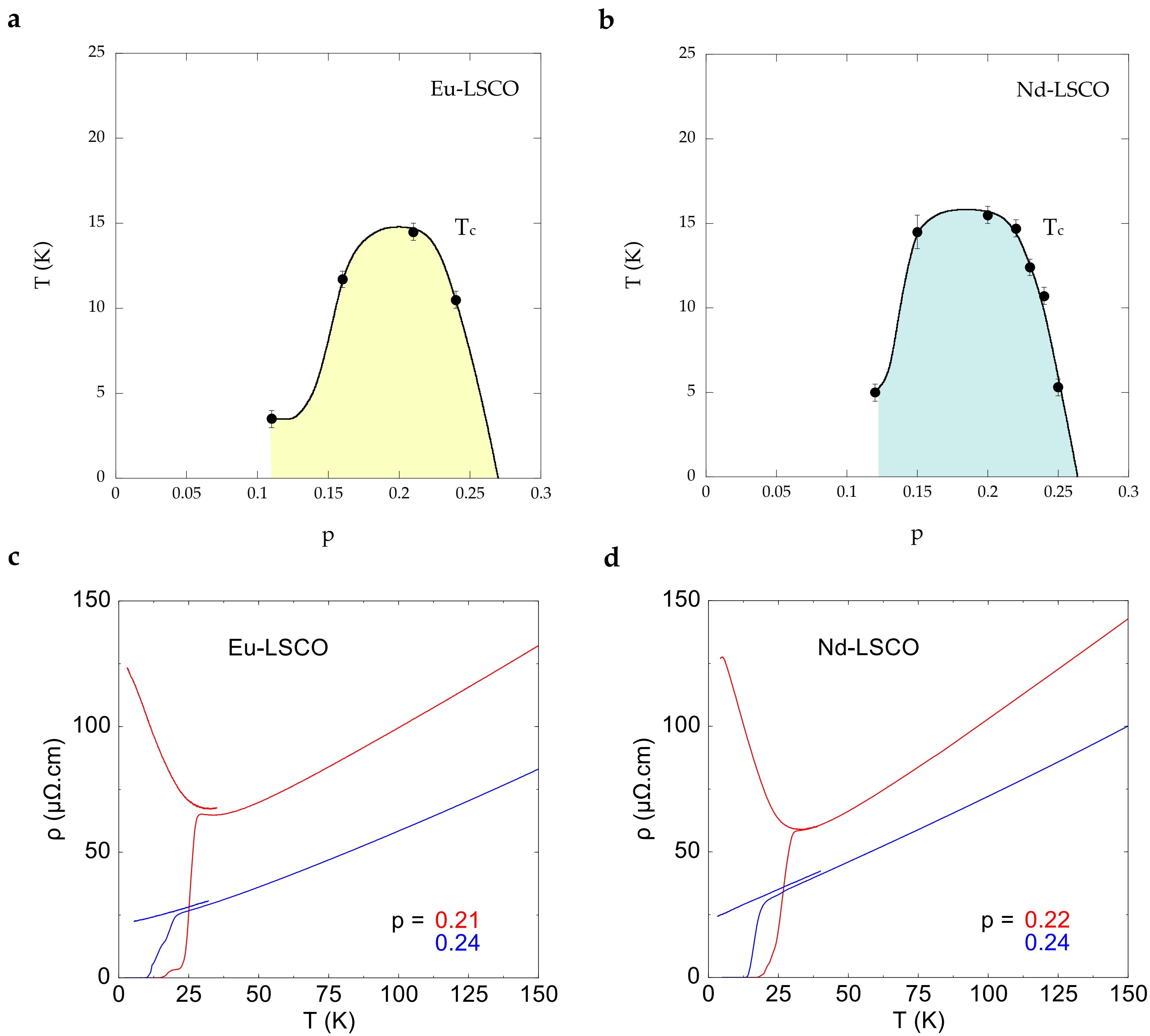

Extended Data Figure 3

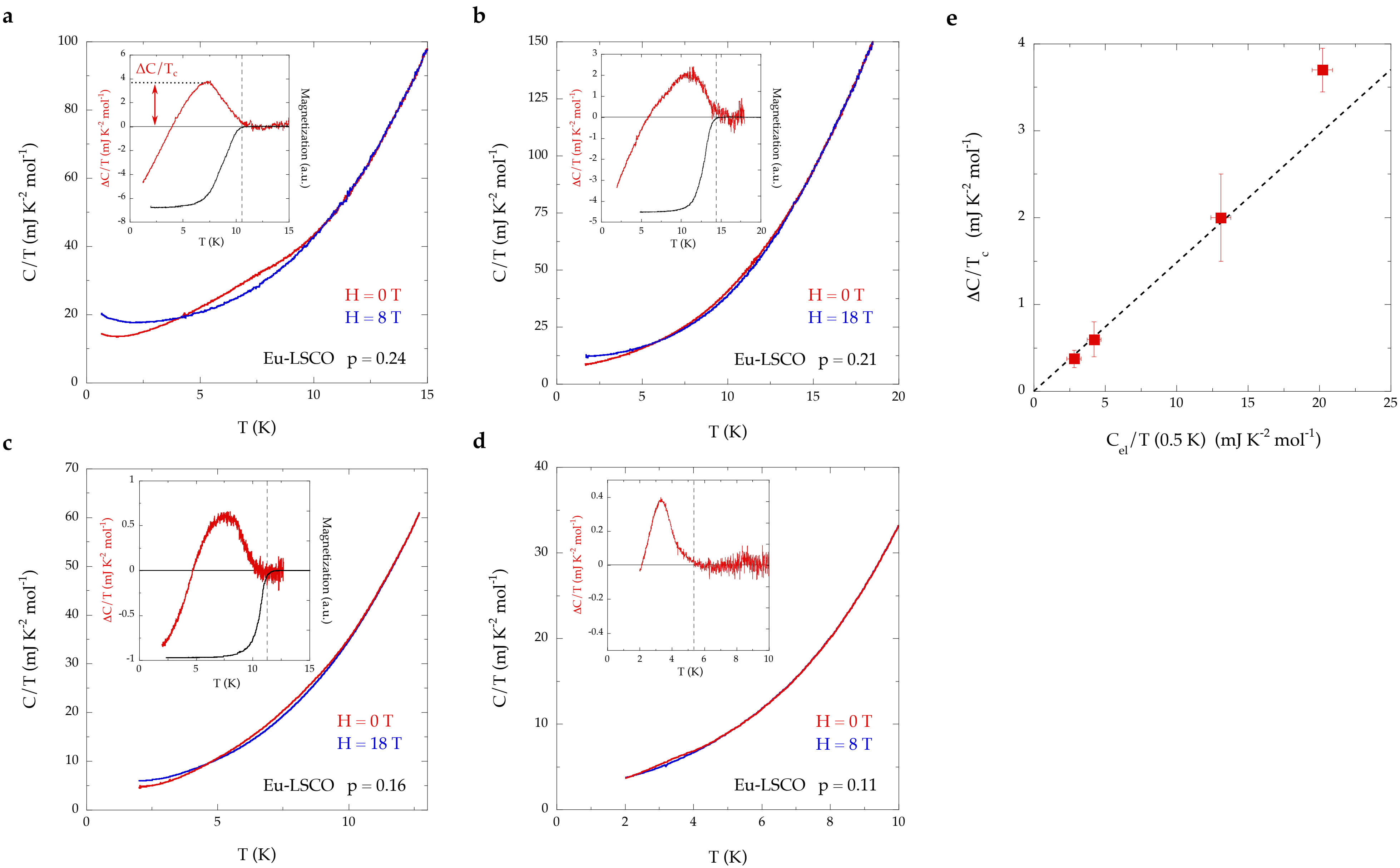

Extended Data Figure 4

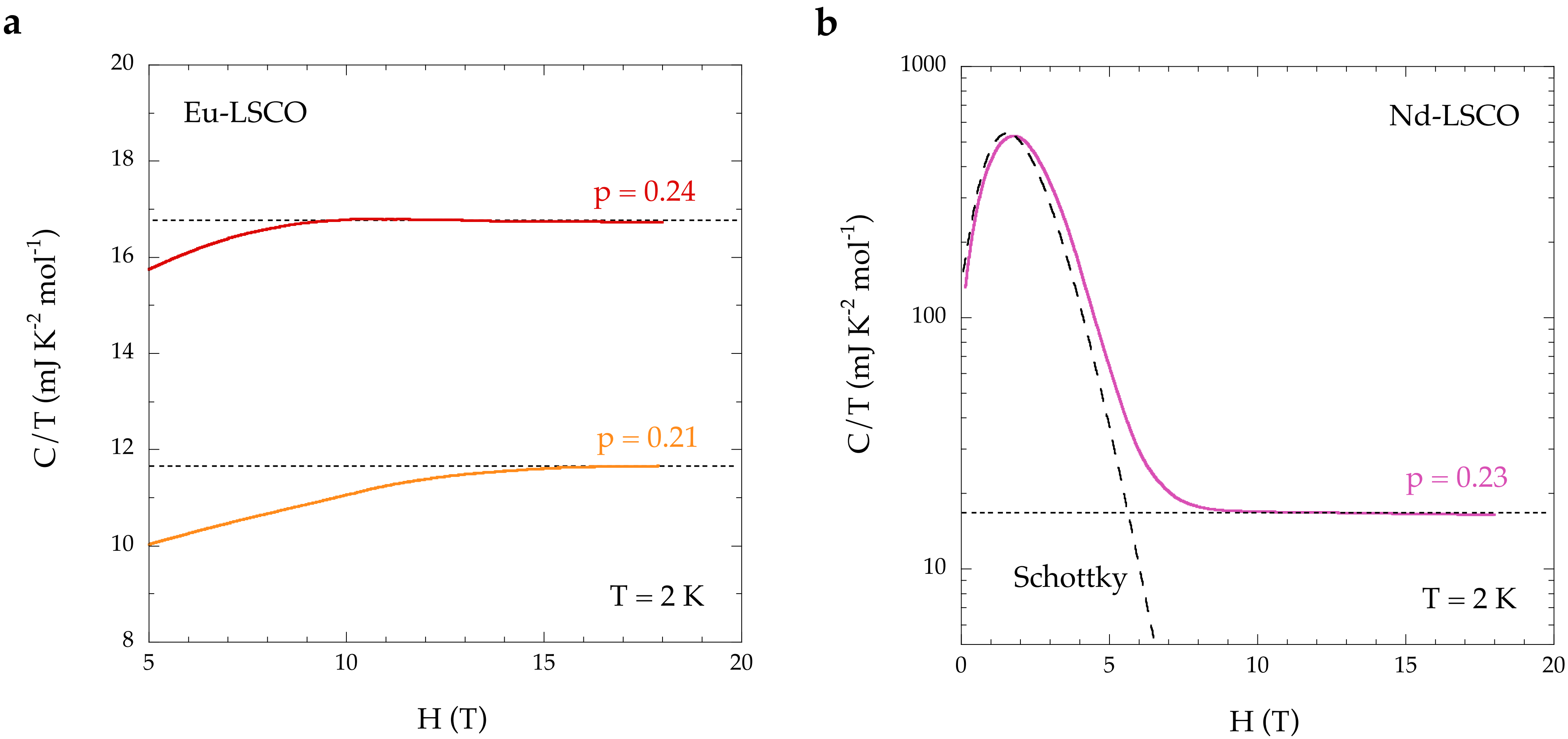

Extended Data Figure 5

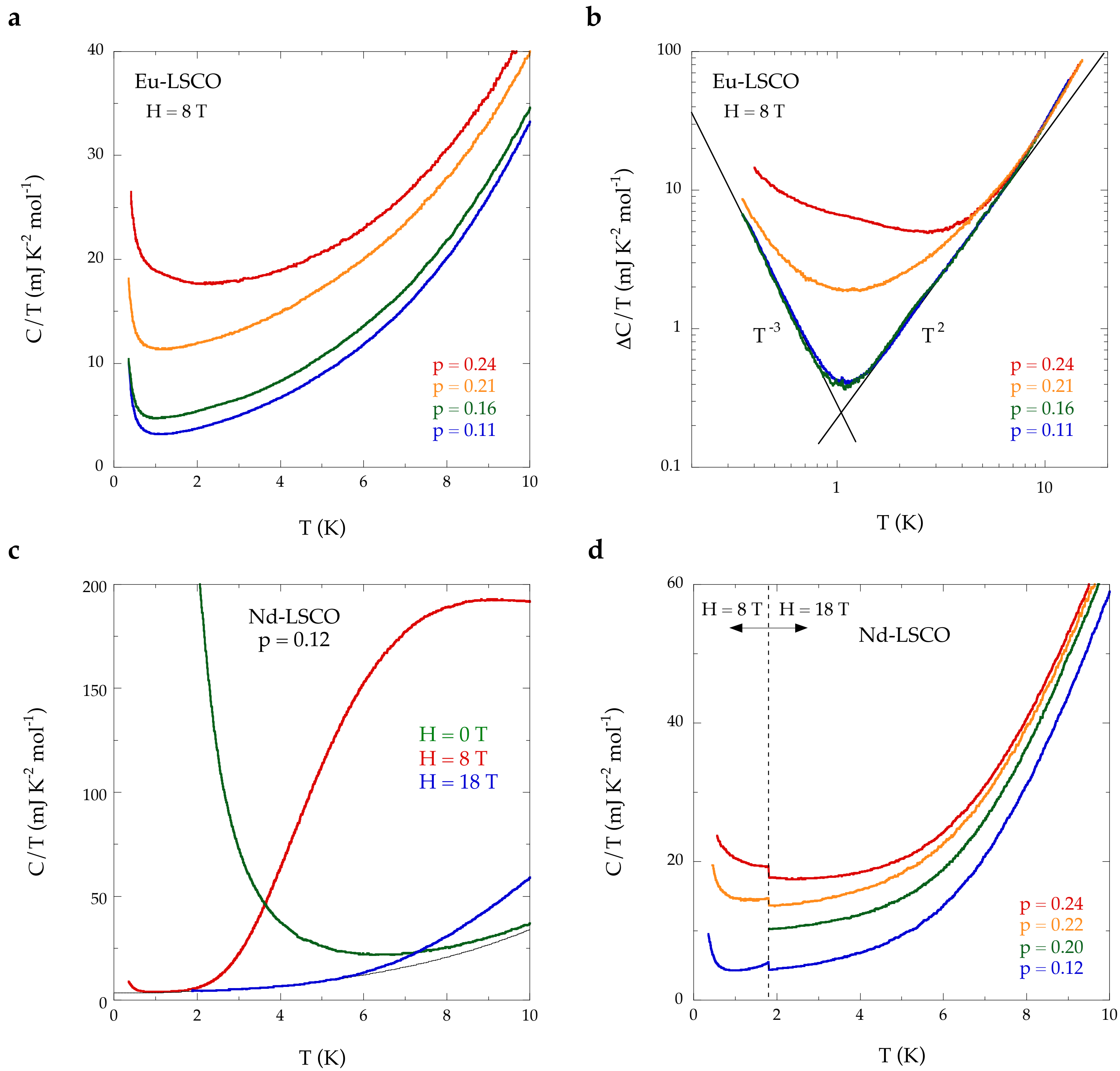

Extended Data Figure 6

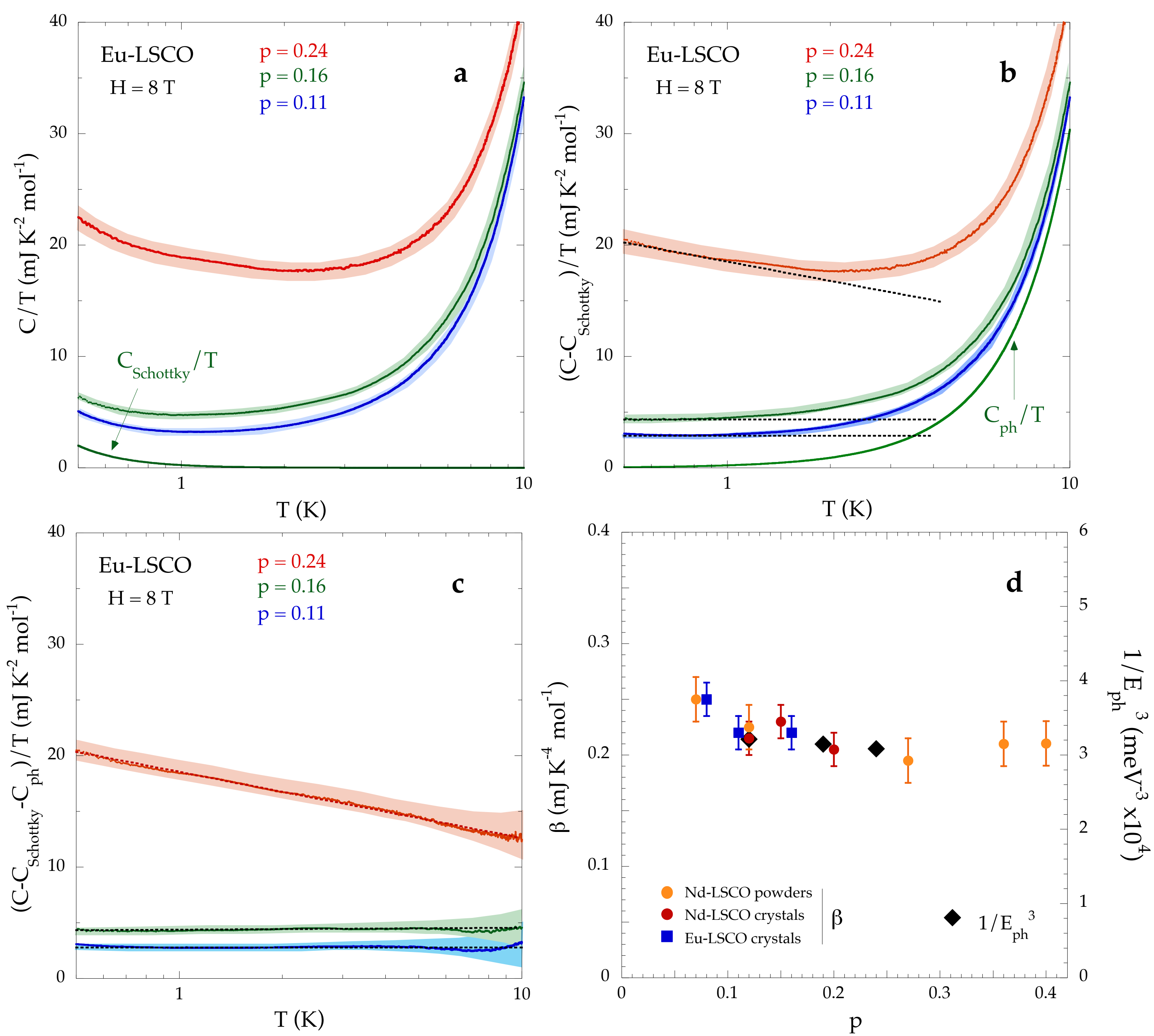

Extended Data Figure 7

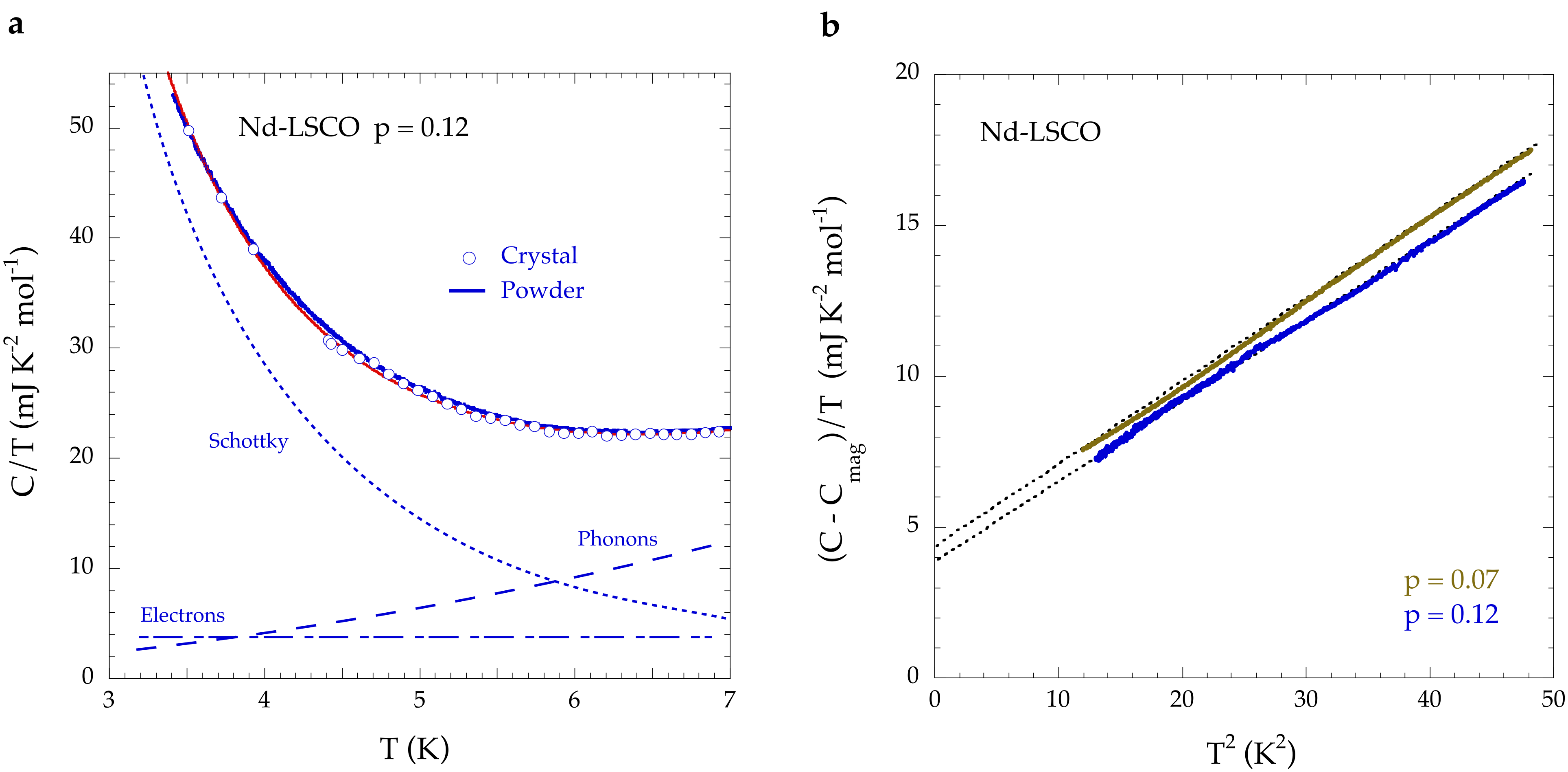

Extended Data Figure 8

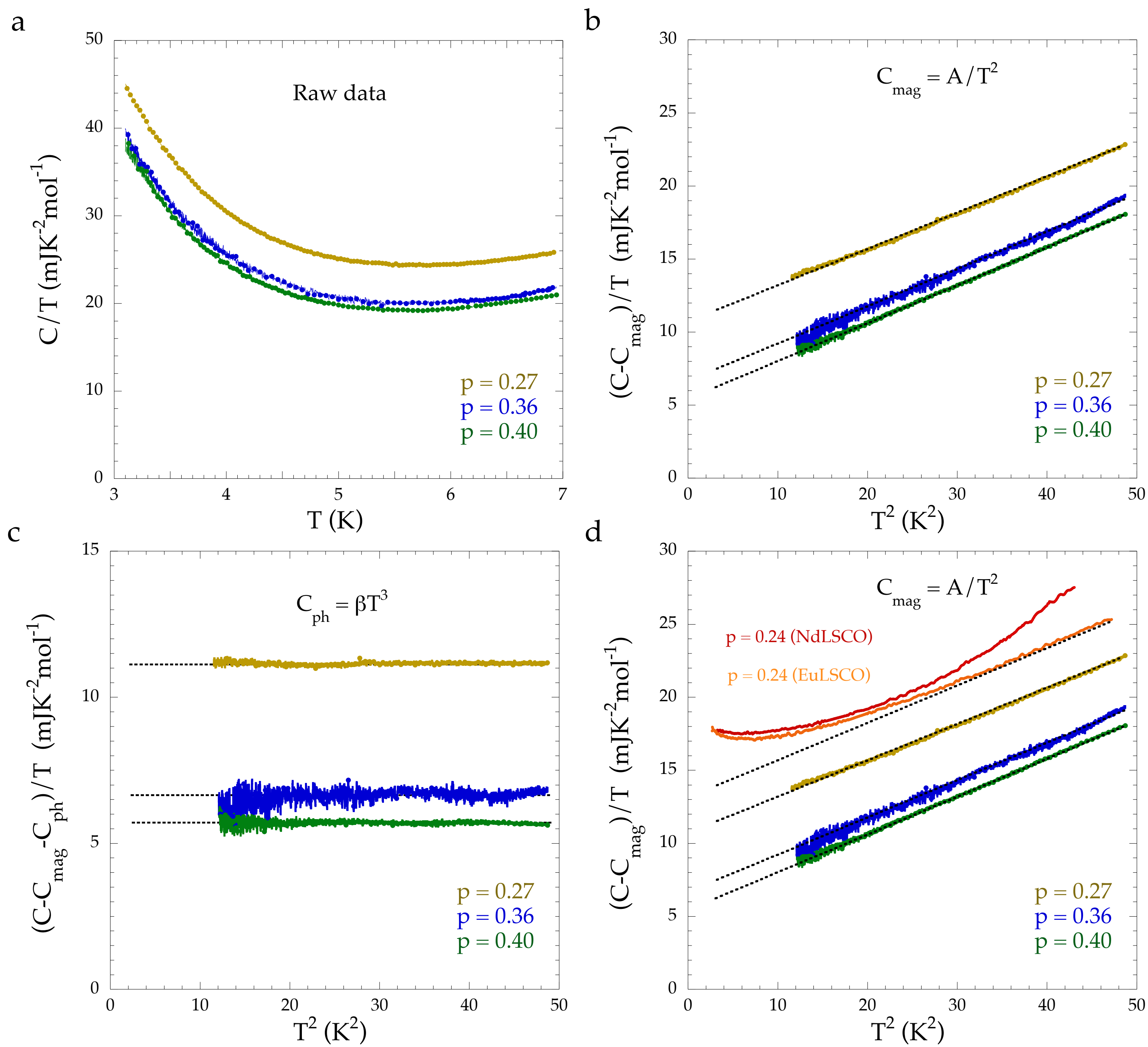

Extended Data Figure 9

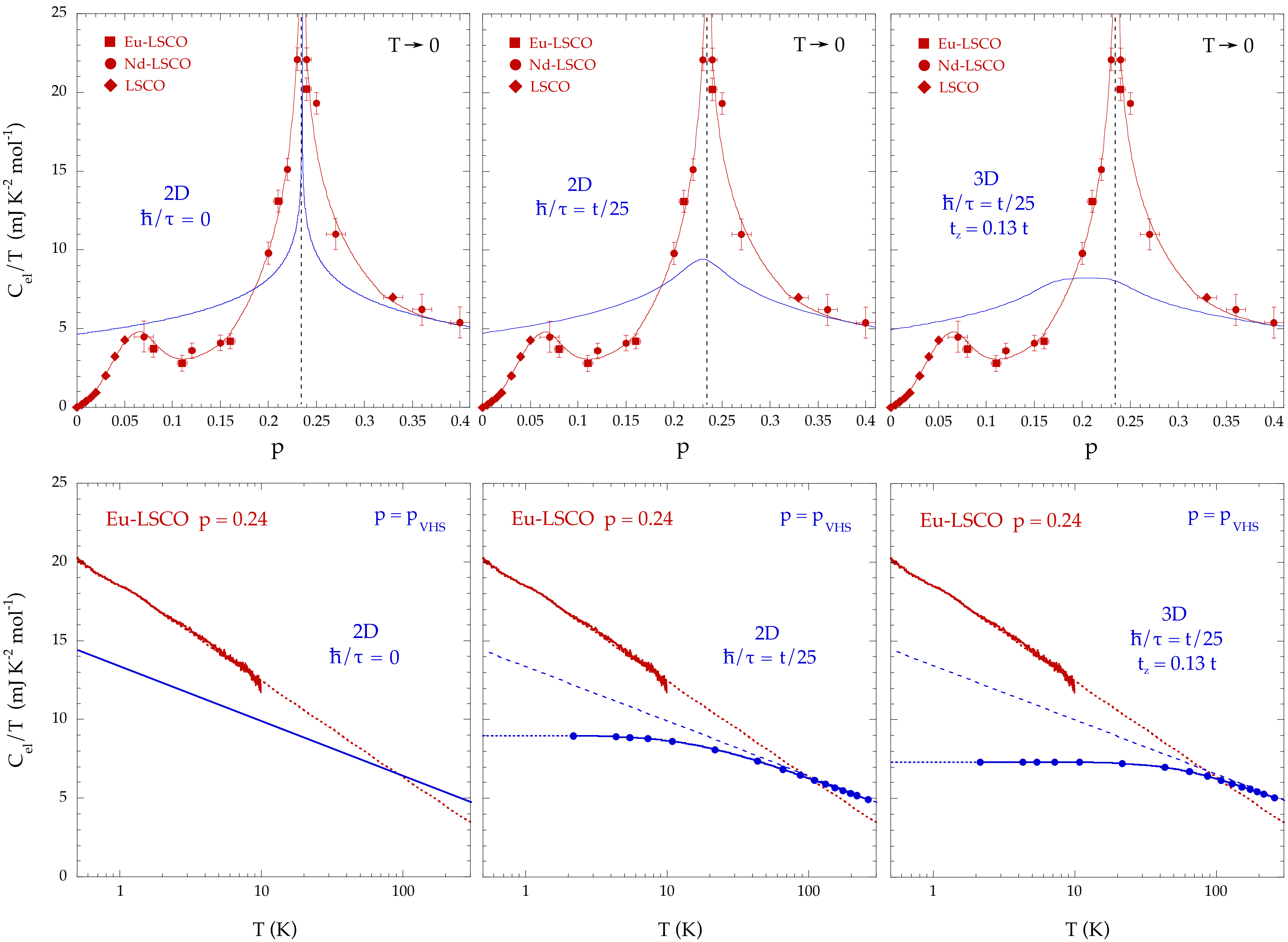

Extended Data Figure 10

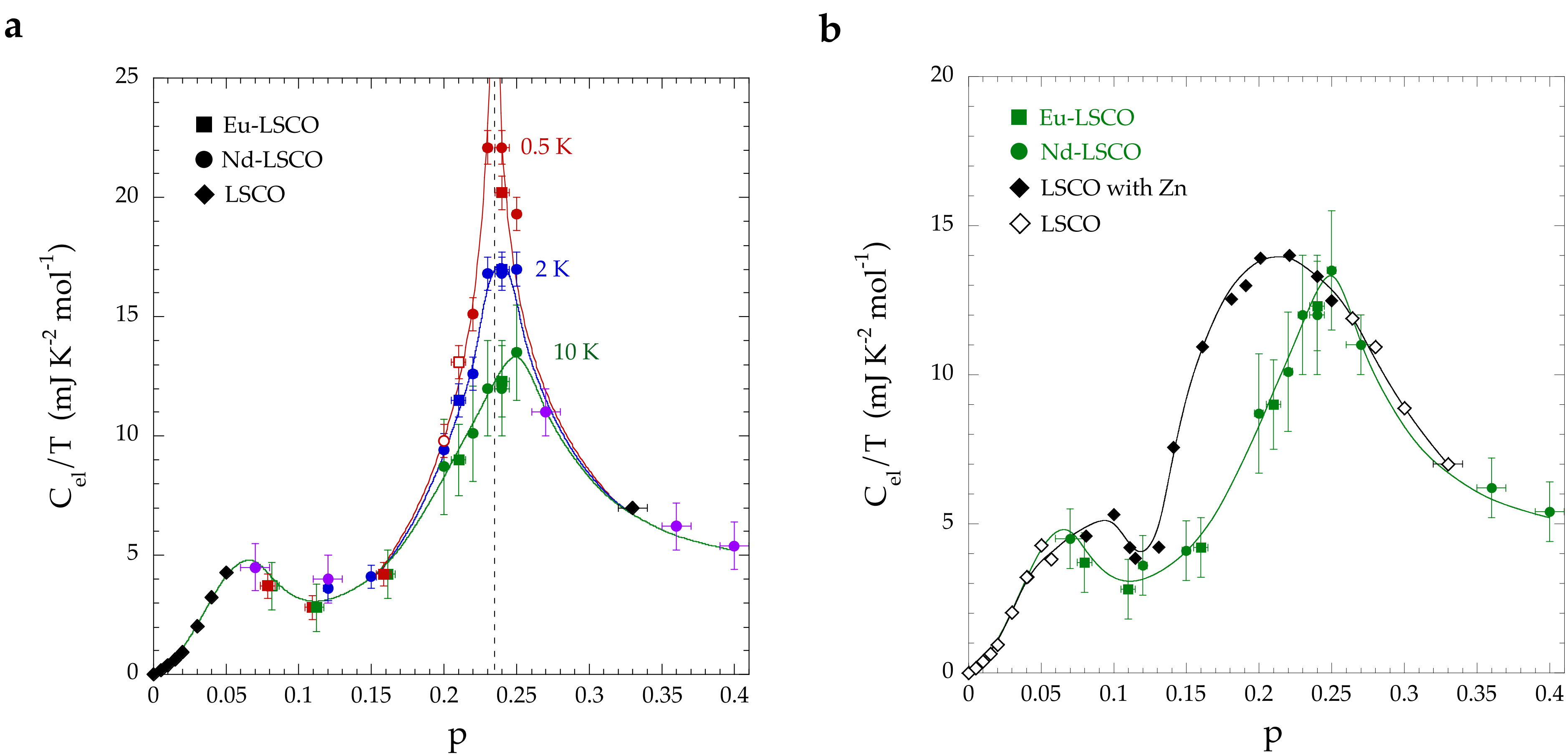

SUPPLEMENTARY INFORMATION

Thermodynamic signatures of quantum criticality in cuprate superconductors

B. Michon *et al*.

CONTENTS

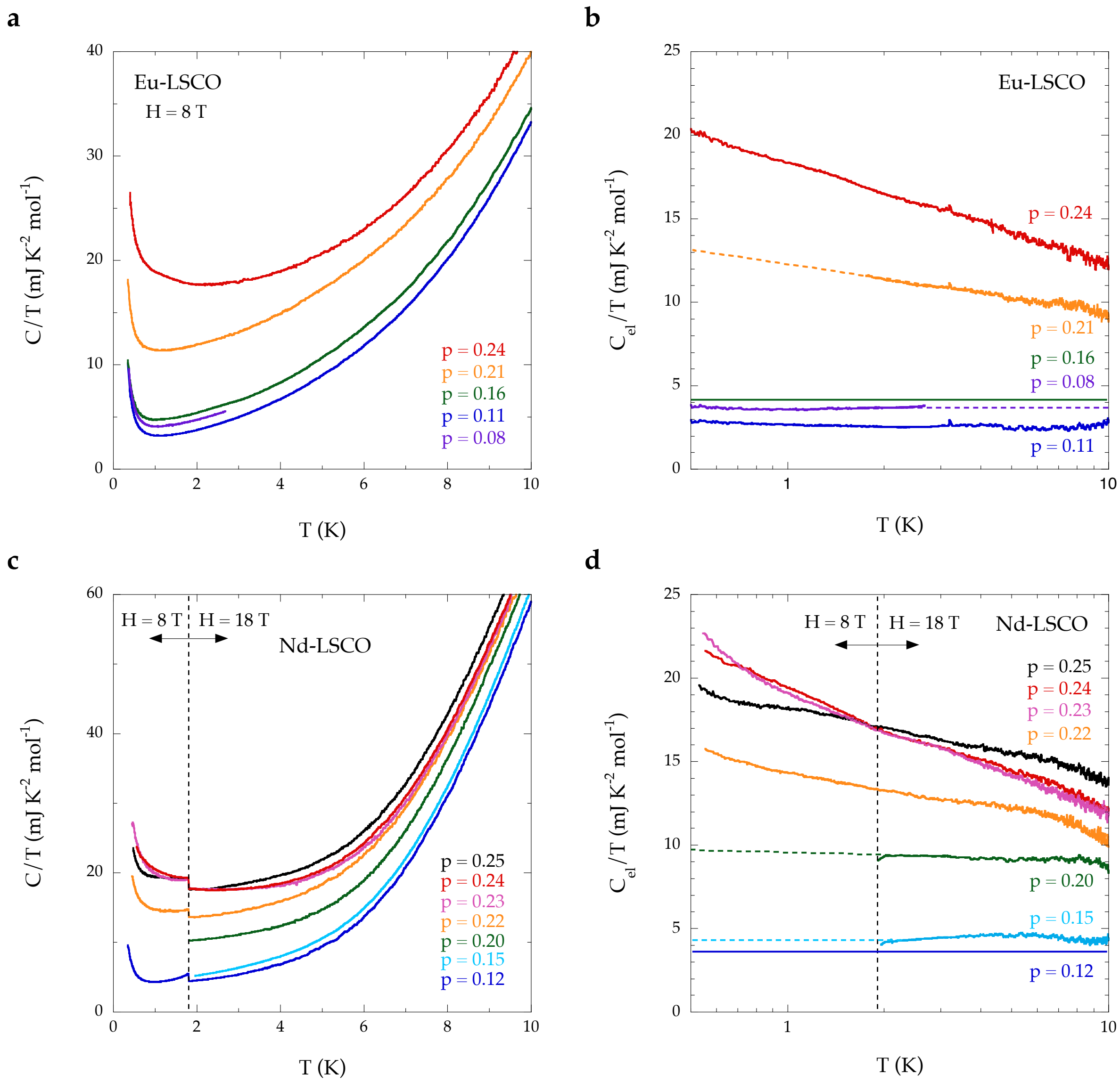

Fig. S1 | Specific heat data for all crystals of Eu-LSCO and Nd-LSCO.

a) Specific heat of our five Eu-LSCO crystals measured in a field H = 8 T, down to 0.4 K. The rapid rise below 1 K is a nuclear Schottky anomaly (C_{nuclear}). **b)** Electronic specific heat $C_{\mathrm{el}}(T)$ of those five Eu-LSCO crystals, plotted as C_{el}/T vs log$T$, from data at H = 8 T (p = 0.08, 0.11, 0.16, and 0.24) and at H = 18 T (p = 0.21). $C_{\mathrm{el}}(T)$ is defined as $C_{\mathrm{el}}(p; T) = C(p; T) - C(p{=}0.16; T) + \gamma$, where γ = 4.2 mJ /K^2 mol is the residual linear term of the p = 0.16 reference data ($C / T = \gamma + \beta T^2$, in Fig. 2a). Dashed lines are a linear extrapolation of the data (p = 0.21, orange; p = 0.08, purple). **c)** Same as panel **a**, for our seven Nd-LSCO crystals (H = 8 T, below the dashed line; H = 18 T, above the dashed line). **d)** Same as panel **b**, for those seven crystals, using data at p = 0.12 as the reference curve for subtraction, with γ = 3.6 mJ /K^2 mol (Fig. 2c).

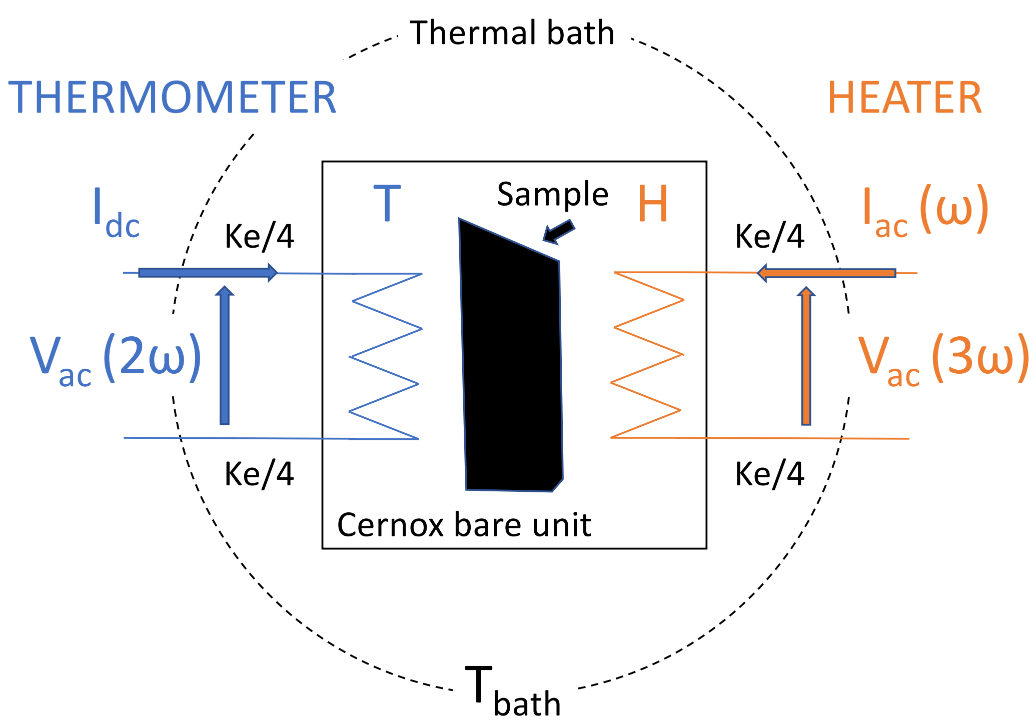

Fig. S2 | Experimental setup for the measurement of heat capacity.

Sketch of our experimental setup, showing the bare Cernox chip (black square) suspended by four PtW wires. A shallow groove is made with a wire saw to obtain two independent sides, one for the heater (H, right side) and one for the thermometer (T, left side). The sample is glued with a minute amount of Apiezon grease on the back of the sapphire substrate. An AC current I_{ac} at a frequency ω is applied across the heater to induce temperature oscillations of the small platform (sample + Cernox). A DC current I_{dc} is applied across the thermometer whose voltage is demodulated at 2ω (see Methods – SPECIFIC HEAT MEASUREMENTS).

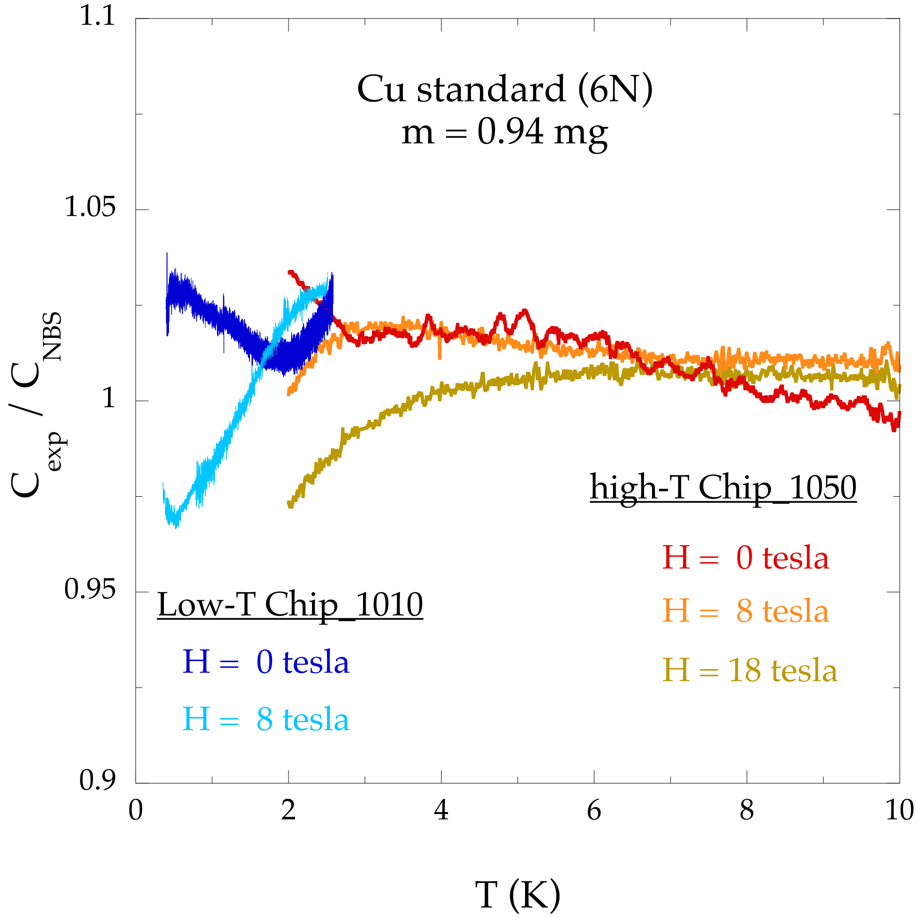

Fig. S3 | Test of our specific heat measurement on a Cu sample.

Specific heat C_{exp} of a sample of copper measured using the same setup and analysis as used for our samples of Eu-LSCO and Nd-LSCO, plotted as C_{exp} / C_{NBS} vs T, where C_{NBS} is the standard value of the specific heat of copper established by the National Bureau of Standards. The measured data never deviate by more than 2-3 % from the standard, over the full temperature range from 0.5 K to 10 K, whether taken in the ^{4}He refrigerator at H = 0, 8 and 18 T (using a Cernox 1050 thermometer) or the ^{3}He refrigerator at H = 0 and 8 T (using a Cernox 1010 thermometer).